BRILLOUIN SCATTERING INVESTIGATION OF GLASS-LIKE PROPERTIES IN $(KBr)_{1-x}(KCN)_x$ MIXED CRYSTALS

BRILLOUIN SCATTERING INVESTIGATION OF GLASS-LIKE PROPERTIES IN $(KBr)_{1-x}(KCN)_x$ MIXED CRYSTALS

by

ZHIBING HU

A Thesis

Submitted to the School of Graduate Studies

in Partial Fulfilment of the Requirements

for the Degree

Master of Science

McMaster University

April, 1985

Master of Science (1985) McMaster University
(Physics) Hamilton, Ontario

Title: Brillouin scattering investigation of glass-like properties in $(KBr)_{1-x}(KCN)_x$ mixed crystals

Author: Zhibing Hu, B.Sc. (Tsinghua University)

Supervisor: Dr. D. Walton

Number of Pages: viii, 71

ABSTRACT

Brillouin scattering technique is used to investigate the transverse acoustic phonon in $(KBr)_{1-x}(KCN)_x$ alloy as a function of temperature for CN^- concentration ranging from 0.20 to 0.50. Anomalies in phonon frequency and linewidth are observed and discussed in terms of coupling of the acoustic phonons with orientational motion of CN^- ions based on a dynamic microscopic model suggested by Michel et al. The frequency and concentration dependence of the freezing temperature, which marks the formation of an orientational glass state, is examined.

A high resolution tandem Fabry-Perot interferometer yields the first evidence of a complex spectrum which consists of the phonon peak and new equal-spaced modes. The Bayesian deconvolution technique is used to extract the spectra. The concentration, time and temperature dependence of these new modes are presented. It is proposed that they arise from the modification of the tunneling levels of the CN, and appear to have the uniform density of states which is the characteristic property of the glass.

ACKNOWLEDGMENTS

I would like to thank my supervisor, Dr. D. Walton, for providing invaluable guidance, help and encouragement throughout the course of this work.

I would also like to thank Drs. D.W. Taylor and J.A. Morrison for many stimulating discussions.

I am grateful to Mr. J. Vanderwal, who has been actively involved in this work, for all his help and uncounted hours of discussions.

I am grateful to Kathy Goodram for her cheerful disposition in typing this thesis under time restraints.

I also wish to express my gratitude to Tsinghua University and McMaster University for their generous financial support.

Finally, thanks to my parents and my wife for their understanding and encouragement.

TABLE OF CONTENTS

LIST OF FIGURES

LIST OF TABLES

CHAPTER 1

INTRODUCTION

Amorphous solids have been studied for a long time. The most surprising property of such materials is due to their universal features at low temperatures. An example is given for liquids which form glasses and crystals with high concentration of magnetic impurities. They are quite different systems. When the temperature decreased, the former will freeze into the disordered state without long range positional order and the latter enter into the spin-glass state with no long range orientational order. At low temperatures, however, they both show similar anomalous behavior in thermal properties, i.e., a specific heat roughly linear in temperature T and a thermal conductivity roughly proportional to T^2.

A phenomenological model proposed by Anderson et al.[1,27] suggested that the universality in glasses arises from a statistical distribution of localized two-level state (TLS). However, there is no satisfactory theory to explain the physical origin of such tunneling states. This disadvantage has hindered the detailed understanding of amorphous solids.

Recently another unusual type of disordered system, $(KBr)_{1-X}(KCN)_X$ with X ranging from 0.1 to 0.56, has attracted a great deal of attention. It exhibits low temperature thermal properties similar to those found in glasses. Since the disorder present can be adjusted by doping with different amounts of CN^- ions, one may expect

that a detailed study of this system will result in understanding the microscopic structure and the low level excitations in glasses.

A wide variety of experimental techniques have been used to investigate $(KBr)_{1-x}(KCN)_x$ mixed crystals. These include: low-temperature specific heat and thermal conductivity[8,24], light scattering[31,37], inelastic neutron scattering[8,18,29], dielectric response[3,4,19,20] measurements etc. Theoretical models for $(kBr)_{1-x}(kCN)_x$ have been proposed by several authors[9,15,16,22,23,32].

The CN^- ion has a small electric dipole moment (p=0.07 eÅ) and an elastic dipole due to its ellipsoidal shape (major and minor semi-axes $\sim$2.15 Å and 1.78 Å respectively)[13] which will be discussed in chapter 2. The interaction between electric dipoles is weak compared to the elastic dipole interaction[25].

Due to the CN^- ion having the same average size as the spherical Br^- ion, it can replace Br^- ion at random over the entire concentration range from x=0 to x=1. The phase diagram covering the entire concentration is illustrated in Fig. 1.1 which reveals four different regimes: (1) pure KCN with x=1, (2) the high concentration range with $0.56 < x < 1.0$, (3) the intermediate concentration range with $0.1 \leq x \leq 0.56$, and (4) the dilute range with $x \leq 0.1$.

Pure KCN crystals undergo a first order transition from a cubic structure with the CN^- ions randomly distributed along <111> directions to a monoclinic structure with CN^- ions aligned along one of the <110> directions at 168°K. That is, below 168K, the CN^- ions are locked into a ferroelastic phase in which cyanides may align

Fig. 1.1: Phase diagram for $(KBr)_{1-x}(KCN)_x$. The "X" line denotes the transitions between disordered and orientational glass phase which depends on probe frequency. The dashed line indicates unknown extent of the antiferroelectric phase after Moy et al.[24]

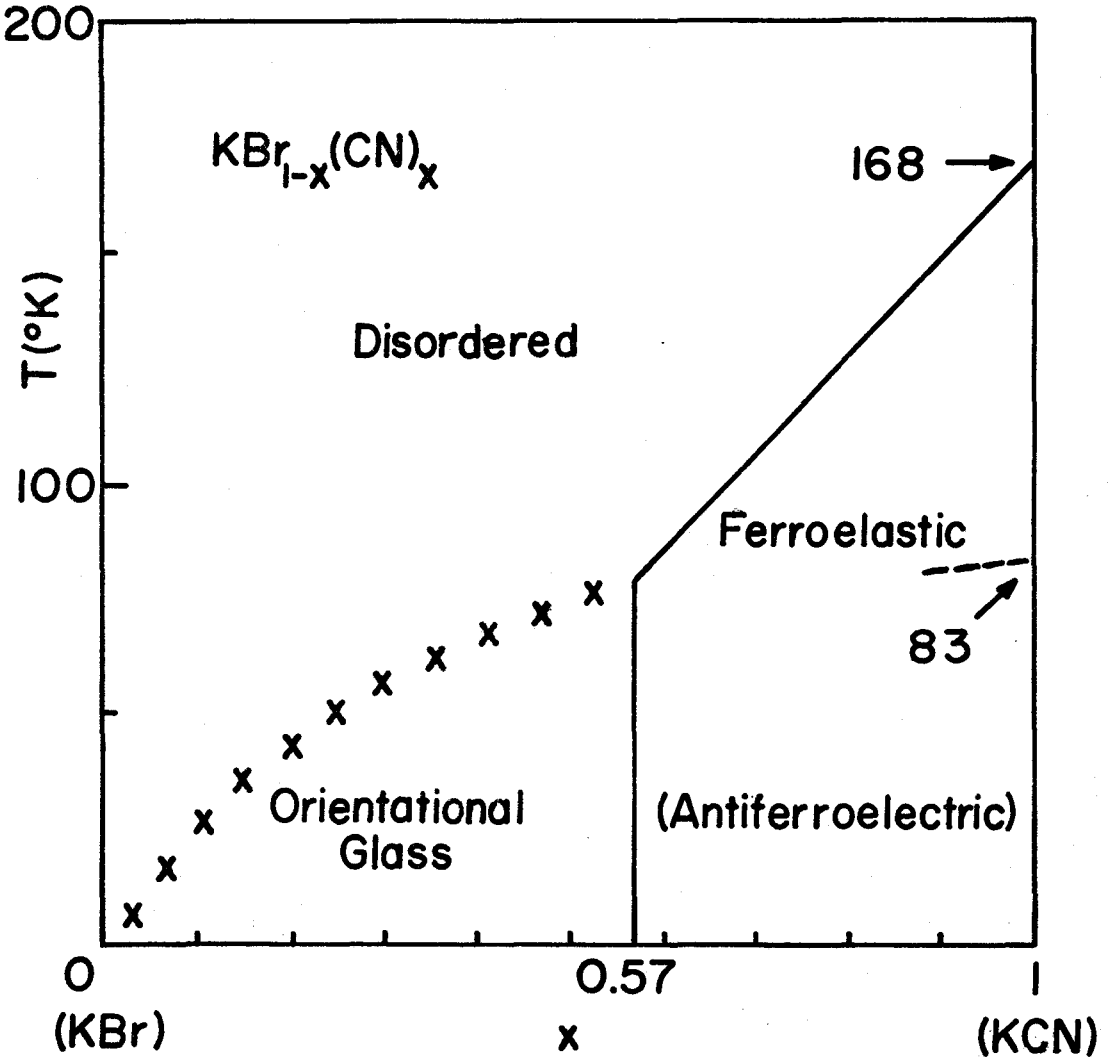
200
100
T(°K)
KBr1-x(CN)x
168
Disordered
Ferroelastic
83
Orientational
Glass
(Antiferroelectric)
0
(KBr)
0.57
x
1
(KCN)

themselves in either CN or NC order. When the temperature reaches 83K, pure KCN will become antiferroelectrically ordered due to the CN, NC degeneracy being lifted by the electric dipole interaction.

The first order transition temperature will decrease on substituting Br^- ions in the KCN lattice until a critical CN^- concentration (X_c=0.57) is reached. Below X_c, no structural phase transitions have been observed. But the crystals will freeze in an orientational glass state analogous to the spin-glass in magnetic systems with decreasing temperatures. The beginning of the frozen state is marked by the freezing temperature T_f. We will see latter that T_f is dependent on the frequency of the probe.

The formation of an orientational glass state due to the interaction among CN^- dipoles is suggested: In the dilute case, the distance between CN^- dipoles is very large and the interaction can be neglected. The CN^- rotors align along <111>-axes in the octahedral crystal field of kBr. The ground state of the CN^- ion is eight fold degenerate which will be partially lifted by quantum mechanical tunneling. When the CN concentration increases, the interaction among CN^- dipoles becomes stronger. The initial tunneling energy levels may be severely modified so that the broad energy spectrum of two level state occurs, which is the characteristic property of the glass.

The present work investigates the glass-like properties in $(KBr)_{1-x}(KCN)_x$ with $0.20 < x < 0.50$ by the Brillouin scattering technique. The transverse acoustic phonon frequency and linewidth were measured and they both showed anomalies i.e. phonon frequency

has a minimum value and phonon linewidth reaches a maximum value at the freezing temperature which marks the formation of an orientational state. The experimental data are compared with the theoretical calculation of Michel et al.[22] The results show that the theory is qualitatively right but quantitatively wrong. The data were also used to compare with other values of the freezing temperature obtained by different frequency probes.

With a high resolution tandem multi-pass Fabry-Perot interferometer, we observed the complex spectrum which consists of the phonon peak and equal-spaced new modes for the first time. These new modes were examined as a function of time, concentration and temperature. A possible explanation is presented which suggests the new modes arise from the modification of the tunneling states in $(KBr)_{1-x}(KCN)_x$.

Chapter 2 is concerned with background theory which discusses the dynamic microscopic model of KBr:KCN system and the translation-rotation coupling proposed by Michel et al.[22] The concept of the elastic dipole will be introduced and a numerical calculation of the interaction energy for an elastic dipole pair will be presented. The basic principles of Brillouin light scattering and Bayesian deconvolution are also discussed.

Chapter 3 describes the experimental techniques which include an introduction to the tandem multi-pass Fabry-Perot interferometer, experimental arrangement, sample preparations, and procedure to measure the Brillouin spectra. Statistical and instrumental errors are examined carefully.

In chapter 4 experimental results are presented and discussed at length. The data are compared with the theoretical results. The new evidence for low energy excitations in KBr:KCN is reported and a semi-quantitatively calculation is presented.

Finally in chapter 5, results are summarized and future experiments are suggested.

CHAPTER 2

BACKGROUND THEORY

2.1 Renormalized frequency of T_{2g} phonon

In $(KBr)_{1-x}(KCN)_x$ mixture systems the frequency of the T_{2g} phonon which propagates in [110]-direction and polarizes in [001]-direction is renormalized. In Chapter 4 we will see that the frequency decreases with decreasing temperature, reaches a finite minimum value and then increases with decreasing temperature. In addition, the shape of the neutron scattering spectra[29] changes as a function of decreasing temperature from the two peak structure to the three peak structure. The purpose of this section is to give a theoretical description of these features in the framework of the microscopic dynamic theory developed by Michel et al.[21,22]

The CN^- ion is idealized as a dumbbell rotor lying on a Fcc lattice of KBr. The two ends of each dumbbell interact with the K^+ ions in octahedral positions by a Born-Mayer potential. This potential depends on the orientation of the dumbbell as well as on the center of mass position of the dumbbell and the six surrounding K^+ ions. By expanding this potential in terms of small displacements from equilibrium positions for all particles, a Hamiltonian with translational and rotational degrees of freedom and a coupling between these motions is obtained.

The full Hamiltonian may be written as

$$H = K^T + V^T + K^R + V^R + V^{TR} \tag{2.1}$$

where the first two terms represent the pure translational energy. The third term is the kinetic energy of rotation. The orientational potential V^R describes the motion of a CN^- in a rigid octahedral environment. Expanding this potential in terms of cubic harmonics, one may obtain the Devonshire potential V^0 as a first term in this expansion[7]. The last term describes the translation-rotation coupling[21]

$$V^{TR} = \sum_i \sum_j{}' \sum_{\alpha=1}^{5} Y_\alpha(\Omega_i) V_\alpha^{(2)} (X_j^+ - X_i^-) U_j^+ + O(Y^4) \qquad (2.2)$$

where Y_α, with α=1-5, are linear combinations of spherical harmonics Y_ℓ^m of order ℓ=2. Ω_i represents a polar angle of the CN^- rigid rotor. X_j^+ and X_i^- are the equilibrium positions of the jth K^+ ion and the ith CN^- ion, and U_j^+ and U_i^- are the deviations from these equilibrium positions. $V_\alpha^{(2)}$ is the coupling matrix in real-space. i runs over all the CN^- ions in the lattice and j runs over all six neighboring K^+ positions for a given ith CN^- ion. Starting from eq. (2.2) and using Fourier transforms[21], one may obtain an effective orientational interaction of the form

$$C_{eff} = -\frac{1}{2} \sum_{\bar{k}} Y_\alpha(\bar{k}) C^{\alpha\beta}(\bar{k}) Y_\beta(\bar{k}) \qquad (2.3)$$

where $Y_\alpha(\bar{k})$ and $Y_\beta(\bar{k})$ respresent the CN^- rotations in reciprocal lattice space and $C^{\alpha\beta}(\bar{k})$ is the CN^- - CN^- coupling matrix. The indirect interaction between two CN^- ions is mediated by lattice deformation. One may draw an analogy with a superconductor where the electron-phonon interaction causes an effective electron-electron

interaction.

In order to calculate the spectral differential cross section, the susceptibility is defined by the Fourier transform of the retarded Green's function for operators $Y_\alpha(\bar{K})$ and $Y_\beta(\bar{K})$ and written as

$$X_{\alpha\beta(\omega)} = (Y_\alpha, Y_\beta)$$

$$= i \int_0^\infty dt e^{i\omega t} \langle [Y_\alpha^t(t), Y_\beta(0)] \rangle \tag{2.4}$$

where $\langle\rangle$ denotes the equilibrium thermal average and α and β run over from 1 to 5.

Besides effective interaction, the rotating CN^- experiences the Devonshire potential V^o. Using molecular-field theory with potential $V = V_{eff} + V^o$, Michel et al. found[22]

$$X_{44}^R = \frac{y}{T}, \quad X_{11}^R = \frac{x}{T} \tag{2.5}$$

with

$$X = \frac{Tr(\exp(-V^o/T)\ Y_3^* Y_3]}{Tr[\exp(-V^o/T)]} \tag{2.6}$$

$$y = \frac{Tr[\exp(-V^o/T) Y_1^* Y_1]}{Tr[\exp(-V^o/T)]} \tag{2.7}$$

The relationship between the susceptibilities and orientation relaxation matrix λ is given by

$$\lambda_1 = \lambda_2 = \frac{\Lambda_{44}}{X_{44}} \tag{2.8}$$

$$\lambda_3 = \frac{\Lambda_{11}}{X_{11}} \tag{2.9}$$

where Λ_{44} and Λ_{11} have a characteristic temperature dependence in three different regimes[21]:

$$\begin{aligned} &(a)\ \Lambda = \Lambda_\infty && \text{for } T > 100K \\ &(b)\ \Lambda = \Lambda_\infty \ell n(\tfrac{T}{25})(\ell n 4)^{-1} && \text{for } 25 < T \leq 100K \\ &(c)\ \Lambda = \Lambda_0 = 0 && \text{for } T < 25K \end{aligned} \tag{2.10}$$

X_{44} and Λ_{44} are defined with functions Y_4 of T_{2g} symmetry while X_{11} and Λ_{11} are defined with functions Y_1 of E_g symmetry. From now on, we only consider the properties dealing with T_{2g} symmetry.

The relaxation function is given[22] by

$$\Phi_{\alpha\beta} = -\frac{1}{2}\left(X_{\alpha\beta}(Z) - X_{\alpha\beta}(0)\right] \tag{2.11}$$

where $X_{\alpha\beta}(Z)$ is the elastic reorientation susceptibility given by eq. (2.4). If one defines $\Phi''(\omega)$ by writing ($Z=\omega\pm i\varepsilon$, $\varepsilon\to 0$):

$$\Phi''_{\alpha\beta}(\omega) = \frac{1}{2i}\left[\Phi_{\alpha\beta}(\omega+i\varepsilon) - \Phi_{\alpha\beta}(\omega-i\varepsilon)\right] \tag{2.12}$$

$\Phi''(\omega)$ is related to the dynamic correlation function by[22]

$$S_{\alpha\beta}(\omega) = -\omega[1-\exp(-\omega/T)]^{-1}\Phi''_{\alpha\beta}(\omega) \tag{2.13}$$

Since the spectral differential cross section is proportional to the $S_{\alpha\beta}(\omega)$, $\Phi''(\omega)$ is the relevant quantity for the interpretation of inelastic neutron or Brillouin scattering experiments. Later, we will use $\Phi''(\omega)$ to fit our experimental data.

In KBr:KCN mixed crystal Φ'' is explicitly given by[22]

$$\Phi''(\omega) = \frac{\lambda_1\beta_1^2/(\omega^2+\lambda_1^2)}{[\omega^2 - \Omega_1^2 - \frac{\beta_1^2\omega^2}{\omega^2+\lambda_1^2}]^2 + [\frac{\lambda_1\omega\beta_1^2}{\omega^2+\lambda_1^2}]^2} \tag{2.14}$$

with $$\Omega_1^2 = \omega_1^2(1 - \frac{C_A y\delta}{T}) \tag{2.15}$$

$$\beta_1^2 = \omega_1^2 - \Omega_1^2 = \frac{\omega_1^2 C_A y\delta}{T} \tag{2.16}$$

and $$\lambda_1 = \frac{\Lambda T}{y} \tag{2.17}$$

where δ is the constant related to the eigenvalue of the effective coupling matrix $\bar{\bar{C}}$. Λ is given by eq. (2.9), C_A is the CN^- concentration. ω_1 is the phonon frequency in pure kBr and ω is renormalized phonon frequency in the presence of effective orientational interaction.

The resonances of $\Phi''(\omega)$ are obtained by setting the denominator of $\Phi''(\omega)$ zero i.e.,

$$\omega^2 - (\Omega_1^2 + \frac{\omega^2\beta_1^2}{\omega^2+\lambda_1^2}) + \frac{i\omega\lambda_1\beta_1^2}{(\omega^2+\lambda_1^2)} = 0 \tag{2.18}$$

Solving this complex equation with the CYBER computer one may obtain the complex ω. Depending on whether the orientational relaxation λ is fast or slow in comparison to a renormalization phonon frequency ω, eq. (2.18) leads to two different regimes:

(1) For fast relaxation, $\lambda_1 > \omega$, there are only two Brillouin resonances. When temperature decreases, the phonon frequency decreases due to coupling becoming stronger.

(2) For slow relaxation, $\lambda_1 < \omega$, there are three resonances, Stokes and anti-Stokes Brillouin peaks as well as a central peak. Due to the decrease of relaxation frequency λ_1 with decreasing temperature, the phonon will decouple with rotating CN^- ions and its frequency will approach that in the pure kBr crystal.

The numerical results for the renormalized T_{2g} phonon frequency with further discussions will be given in Chapter 4.

2.2 Interaction of an elastic dipole pair

In dilute $(KBr)_{1-x}(KCN)_x$ systems the effective interaction between cyanide dipoles may be neglected. CN^- ions align along <111>-axes in the Octahedral crystal field of kBr[25]. Since there are eight equivalent <111> directions, the CN^- ground state is eight-fold degenerate. However the CN^- wave functions are sufficiently extensive for overlap to occur, and quantum mechanical tunneling becoming important. Hence the ground state will be split into 4 tunneling states. An approximate level scheme is shown in fig. 2.1(a) after Loidl[18]. The energy levels are labelled according to the irreducible representations of the octahedral group O_h. The arrows indicates quadrupolar transitions with T_{2g} and E_g symmetries. In this research, we focus on transitions of T_{2g} symmetry.

When the concentration of CN^- ion increases, the tunneling levels may be significantly modified by the interaction between CN^- ions. Fisher and Klein[9] first proposed a two-dimensional model which suggested that the KBr:CN system may produce very similar low temperature thermal properties to those observed in amorphous

Fig. 2.1(a): Approximate level scheme of a rigid CN^- dumbbell in an octahedral hindering potential of kBr after Loidl et al.[18] The arrows indicate that there is strong coupling between these tunneling excitations and the T_{2g} as well as E_g symmetry phonons.

Fig. 2.1(b): Scheme of a strain ellipsoid of the λ-tensor after Nowick et al.[26] λ_1, λ_2 and λ_3 are referred to as the principal values of the λ-tensor.

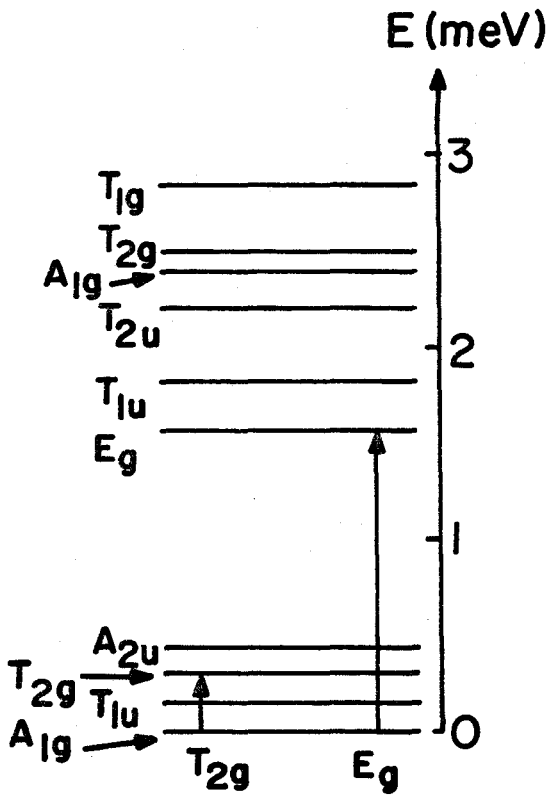

(a)

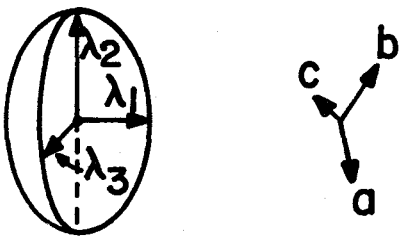

THE STRAIN ELLIPSOID

THE CRYSTAL AXES

(b)

solids when strain interactions between CN^- ions are considered. This section will present a calculation of interaction energy of a CN^- pair based on Nowick and Hellen's theory[26]. In chapter 4 we will see that this interaction will result in new modes which may be used to explain the low-temperature thermal properties of KBr:KCN systems.

The concept of an "elastic dipole" is introduced by analogy to the electric dipole. Considering the interaction energy of an electric dipole $\bar{\mu}_{elec.}$ with an electric field $\bar{E}$ is written as

$$\mu_{elec.} = -\sum_i \mu_i E_i \qquad (i=1,2,3) \tag{2.19}$$

the interaction energy of a dumbbell shaped defect with a stress field $\bar{\bar{\sigma}}$ may be defined by

$$\begin{aligned} \mu_{elas.} &= -\sum_{ij} v_{ij}\, \sigma_{ij} \\ &= -v_o \sum_{ij} \lambda_{ij}\, \sigma_{ij} \end{aligned} \tag{2.20}$$

where V_{ij} is referred to as the components of the elastic dipole. Since v_{ij} have dimensions of volume, it is convenient to introduce the dimensionless quantity λ_{ij} by factoring out the atomic volume, V_o, of the host crystal KBr. The interaction energy must be a scalar and stress a tensor, hence the elastic dipole is described by a second-rank tensor. As with any strain tensor it is possible, by rotating the coordinates, to find orthogonal principal directions in which the tensor only has values in diagonal elements:

$$\bar{\bar{\lambda}} = \begin{vmatrix} \lambda_1 & 0 & 0 \\ 0 & \lambda_2 & 0 \\ 0 & 0 & \lambda_3 \end{vmatrix}$$

where the quantities λ_1, λ_2 and λ_3 are called the principal values of the λ-tensor which basically represent the shape of the elastic dipole. A strain ellipsoid is illustrated in fig. 2.1(b).

The given elastic dipole "sees" a strain field which has two sources; the first is from application of an external stress field and the other is from internal interaction with the other dipoles in the lattice. Here we only consider interaction energy between two nearest neighbour CN^- ions.

Following Nowick and Heller[26], when a defect is introduced into the lattice, it will cause distortion. The displacement from the equilibrium position falls off as r^{-2} and is given by

$$S = \frac{-pk(1+\nu)}{12\pi(1-\nu)} \text{ grad } (\frac{1}{r}) \tag{2.22}$$

where k and ν are the compressibility and Poisson's ratio of the isotropic elastic material respectively. It can be shown[26]

$$v_o tr\lambda = kP \tag{2.23}$$

where $tr\lambda$ is the sum of the diagonal elements of λ-matrix.

The strain components ε_{ij} are defined by the relations

$$\varepsilon_{ij} = \frac{\partial S_i}{\partial X_j} \tag{2.24}$$

with i, j running from 1 to 3. Hooke's law states that for sufficiently small deformations the strain is directly proportional to the stress, so that the stress components are linear functions of the strain components:

$$\sigma_{ij} = \sum_{kl} C_{ijkl}\, \varepsilon_{kl} \qquad (2.25)$$

The quantities C_{1111}, ... are called the elastic stiffness constants or moduli of elasticity. Considering the symmetry in cubic system there are only three independent stiffness constants. Inserting eq. (2.25) into eq. (2.20) with Voigt notation:

$$11 \to 1,\ 22 \to 2,\ 33 \to 3,\ 23 \to 4,\ 31 \to 5,\ 12 \to 6,$$

one may obtain the interaction energy of an elastic dipole pair:

$$U_{pair} = -V_o \sum_{ij} \lambda_i\, C_{ij}\, \varepsilon_j \qquad (2.26)$$

Substituting eqs. (2.22), (2.24) into eq. (2.26) with the elastic constants for pure KBr, viz

$C_{11} = 4.06$, $C_{44} = 0.627$ and $C_{12} = 0.67$ ($\times 10^{11}$ dyn/cm^2),

Poisson ratio = 0.14, $v_o = 3.106 \times 10^{-23}$ cm^3, nearest neighbor distance = 4.67Å, $\lambda_1 \sim 0.038$ and $\lambda_2 = \lambda_3 \sim 0.10$ obtained by ultrasonic experiments[6], the interaction energy is about 5.2K.

This is only a rough calculation since the appropriate elastic siffness constants in KBr:KCN system are unknown and also eq. (2.22) arises from the model of a dilatational defect in an isotropic elastic solid. However one may obtain the order of the interaction. This

will be discussed further in chapter 4.

2.3 Brillouin light scattering

Light scattering is a well-known technique for investigating the properties of long wavelength elementary excitations in the condensed matter. This field has rapidly developed since the advent of the laser. In our experiments, we use light scattering to study the transverse acoustic phonon in $(KBr)_{1-x}(KCN)_x$ mixed crystal.

As shown in Fig. 2.2(a), a high intensity incident laser beam is scattered by a phonon with a wavevector $\bar{q}$ and angular frequency $\omega_{\bar{q}}$. The wave vector of the photon changes from $\bar{k}_i$ to $\bar{k}_s$ and its frequency from ω_i to ω_s. The conservation of energy and momentum are written as

$$\hbar\omega_s = \hbar\omega_i \pm \hbar\omega_{\bar{q}} \tag{2.27}$$

and

$$\hbar\bar{k}_s = \hbar\bar{k}_i \pm \hbar\bar{q} \tag{2.28}$$

where the positive sign is for an anti-Stokes enent corresponding to a phonon annihilation while the negative sign is for a Stokes event corresponding to a phonon emission.

Because the photon wave vectors (of order of 10^5 cm^{-1}) are small compared with the Brillouin zone dimensions (of order 10^8 cm^{-1}), information is provided only about phonons near $\bar{q} = 0$. The process is referred to as Brillouin scattering, when the phonon emitted or absorbed is acoustic, and Raman scattering, when the phonon is optical. Since the phonon frequency is typically of order of 10-20 GHz and

Fig. 2.2(a): Inelastic scattering of a photon of wave vector $\overline{k}_i$, with the production (Stokes event) or the absorption (anti-Stokes event) of a phonon of wavevector $\overline{q}$. The scattered photon has wavevector $\overline{k}_s$.

Fig. 2.2(b): Selection rule diagram for the process of fig. 2.2(a). If $k \doteq k'$, the triangle is isosceles. The base of the triangle is $k = 2k \sin \frac{\theta}{2}$.

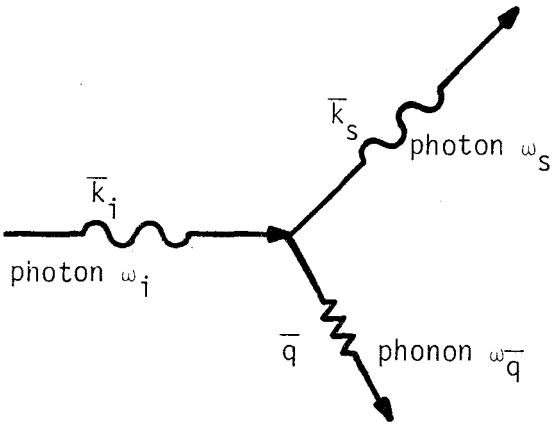

Stokes event

$\bar{k}_s = \bar{k}_i - \bar{q}$

$\omega_s = \omega_i - \omega_{\bar{q}}$

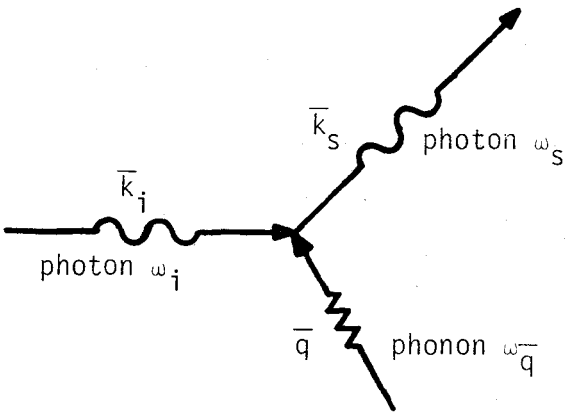

Anti-Stokes event

$\bar{k}_s = \bar{k}_i + \bar{q}$

$\omega_s = \omega_i + \omega_{\bar{q}}$

(a)

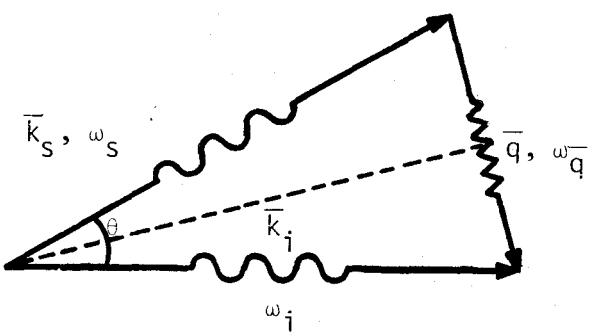

(b)

the incident photon frequency is of the order of 10^5 GHz, one can safely make the assumption

$$\omega_{\bar{q}} << \omega_i$$

Therefore $\omega_i \approx \omega_s$ and $|\bar{k}_i| \doteq |\bar{k}_s|$. The triangle in fig. 2.2(b) is very nearly isosceles. It follows immediately that

$$|\bar{q}| = 2|\bar{k}_i| \sin \frac{\theta}{2} \tag{2.29}$$

where θ is the scattering angle.

The dispersion relation for acoustic phonons with long wavelength is given by

$$\omega_{\bar{q}} = V_{\bar{q}} |\bar{q}| \tag{2.30}$$

where $V_{\bar{q}}$ is the velocity of the phonon with wave vector $\bar{q}$ and frequency $\omega_{\bar{q}}$. For light propagating in the medium,

$$n\omega_{\bar{k}} = C|\bar{k}| \tag{2.31}$$

where n is the refractive index of the solid and C is the velocity of light. From eqns. (2.29), (2.30) and (2.31) it is easy to obtain

$$\omega_{\bar{q}} = \omega_s - \omega_i = \pm 2 \frac{V_q \omega_i n}{C} \sin \frac{\theta}{2} \tag{2.32}$$

which was first derived by Brillouin. The frequency $\omega_{\bar{q}}$ is determined by the measured small change in photon frequency with high resolution instruments such as the Fabry-Perot interferometer.

A spectrum of scattered light will show that a Stokes and an anti-Stokes Brillouin peaks are symmetrically located about the

Rayleigh peak and separated from it by a frequency equal to that of an acoustic phonon. The Rayleigh peak arises from elastic scattering due to nonpropagating entropy fluctuations or diffuse type excitations of solids[11].

2.4 Bayesian deconvolution

In light scattering experiments, the scattered light was analyzed and amplified by the electronic system characterized by a response function R(t,t'). If the relationship between the true signal T[t] and measured spectrum M[t] is governed by a linear differential equation of the form

$$\sum_{n=0}^{\infty} A_n \frac{d^n m}{dt^n} = \sum_{n=0}^{\infty} B_n \frac{d^n T}{dt^n} \tag{2.33}$$

with coefficients A_n and B_n being independent upon time, the system is linear and invariant. R(t,t') can be written as R(t-t'). Physically this condition demands the resistance and capacitance do not vary with time.

Under such a restriction, the measured signal is a convolution of the response function and the true signal and is given by the convolution integral

$$M(t) = \int R(t-t')T(t')dt' \tag{2.34}$$

The extraction of the T(t') by solving the above integral equation is referred to as deconvolution which will enhance the fine structure in the spectra[14].

Mathematically if $T(t')$ is a δ-function, eq. (2.33) yields

$$M(t) = \int R(t-t')\delta(0)\, dt' = R(t) \tag{2.35}$$

This result thus defines the response function to a sharp impulse. Assuming that the incident laser beam is a sharp impulse neglecting its linewidth, the response function can be determined by the Rayleigh spectral function.

In the instance of discrete spectra, the relationship between $T(t)$ and $M(t)$ in the conjugate domain may be written most simply in matrix form as

$$\overline{M} = \bar{\bar{R}}\ \overline{T} \tag{2.36}$$

where $\bar{\bar{R}}$ is the response matrix, and $\overline{M}$ and $\overline{T}$ are vectors.

The Bayesian deconvolution algorithm is based on the concept of conditional probability

$$P(H/D) = \frac{P(D/H)\ P(H)}{P(D)} \tag{2.37}$$

where $p(H)$ is the a priori probability of event H and $P(H/D)$ the a posteriori probability of event H in condition of given event D. Following Kennett et al.'s work[14] one may obtain

$$P(T_i/M_k) = \frac{P(M_k/T_i)P(T_i)}{\sum_j P(M_k/T_j)P(T_j)} \tag{2.38}$$

It is apparent that

$$P(T_i) = \sum_k P(T_i/M_k)\ P(M_k) \tag{2.39}$$

Inserting eq. (2.38) into (2.39), one may obtain

$$P(T_i) = \sum_k \frac{P(M_k/T_i)\ P(T_i)\ P(M_k)}{\sum_j P(M_k/T_j)P(T_j)} \tag{2.40}$$

The term $P(T_i)$ which appears on both sides of eq. (2.38) is the desired solution. Since it is not easy to explicitly represent this term, a beginning function must be estimated. An iterative formula is given by

$$P^{(n+1)}(T_i) = P^{(n)}(T_i) \sum_k \frac{P(M_k/T_i)P(M_k)}{\sum_j P(M_k/T_j)P^n(T_j)} \tag{2.41}$$

Considering that $P(T_i) = \dfrac{T_i}{\sum_j T_j}$,

$$P(M_i) = \frac{M_i}{\sum_j M_j}, \text{ and } P(M_k/T_i) = R_{ki}, \tag{2.42}$$

One obtains immediately

$$T_i^{(n+1)} = T_i^{(n)} \sum_k \frac{R_{ki}\ M_k}{\sum_j R_{kj}\ T_j^{(n)}} \tag{2.43}$$

where $T_i^{(n)}$ is the estimate of T_i after n interactions.

The implementation of the algorithm is accomplished with a computer. It is common procedure to initially set $T^{(0)}$ equal to the measured spectrum, i.e., $\overline{T}^o = \overline{M}$. As noted[33] one is then faced with a very significant running time if the high quality deconvolution with large interation index n is needed.

In order to reduce the running time, one may assume a Lorentzian profile as the starting function whose linewidth is determined by an optimizing subprogram. In this way the iteration cycles are reduced from many hundreds to less than fifty[33,34]. A BASIC program in the Nova computer requires 2 hrs to finish 30 iterations with 200 data channels. For deconvolution process in wide spectral range such as 400 data channels, a FORTRAN program in an Osborne Computer was needed and its running time was 80 mins. for 30 cycles. For both programs, a Lorentzian function was used as the zeroth iteration. Of course, it did not restrict subsequent iteration results.

CHAPTER 3

EXPERIMENTAL TECHNIQUES

3.1 Tandem Multi-pass Fabry-Perot Interferometer (TMFPI)

The multiple-beam interferometer first constructed by C. Fabry and A. Perot in the late eighteen hundreds is a spectroscopic device of extremely high resolving power. It consists of two plane, parallel and highly reflecting mirrors separated by some distance d. A large number of multiply internally reflected rays are generated and result in multiple beam interference which distributes according to an Airy formula[11]

$$I^{(t)} = I^{(i)}(1 - \frac{A}{1-R})^2 \left[\frac{1}{1 + \frac{4R}{(1-R)^2}\sin^2\frac{\delta}{2}}\right] \tag{3.1}$$

where $I^{(t)}$ and $I^{(i)}$ are the transmitted and incident light intensities respectively, A is the absorption coefficient of the mirror, R is the reflectivity and δ is a phase angle between successive reflections.

From the Airy formula it is easy to obtain the constructive interference condition

$$d = \frac{m\lambda}{2} \tag{3.2}$$

where m is integer and λ is the wavelength of the incident beam.

The contrast of the fringes is expressed by

$$C \equiv \frac{I^{(t)}_{max}}{I^{(t)}_{min}} = \left(\frac{1 + R}{1 - R}\right)^2 \tag{3.3}$$

For R $\sim$ 90%, C is on the order of a hundred. To permit frequency scanning, one of the mirrors is rigidly held while the other mirror is moved by means of piezoelectric stacks. A high voltage ramp applied to these stacks then physically changes the distance (d) between the mirrors, the rate of which is determined by the time period of the ramp.

The frequency separation between two neighbouring Rayleigh peaks is called the free spectral range (FSR) which is given by

$$FSR = \frac{C}{2d} \tag{3.4}$$

where C is the velocity of light. The full width at half maximum (FWHM) of the Rayleigh peak, $\delta\nu$, and free spectral range are related to another important parameter, F, which is referred to as the finesse and is given by

$$F = \frac{FSR}{\delta\nu} \tag{3.5}$$

The major factors which limit the finesse are the reflectivity, parallelism and flatness of the mirrors. The limitation can also be caused by the external optics, pinholes etc. In our experiments, F is about 46$\sim$50.

Usually the Brillouin peaks have very low level count rates ($\sim$20 counts/min) and therefore one requires an extremely high contrast factor ($10^{8}\sim10^{12}$). This demand can be satisfied by using a multi-passed interferometer in which the peak transmission and contrast will be the product of those for single interferometer; i.e.

$$I_p^{(t)} = [I^{(t)}]^P, \quad Cp = [C]^P \tag{3.6}$$

where p is the number of passes. In a multi-pass system, the light beam passes through a single interferometer several times by using corner cubes at opposite ends of the interferometer.

The particular value of a tandem multi-pass Fabry-Perot interferometer (TMFPI) arises from the fact that besides increasing contrast of the spectra, it also serves to overcome the order ambiguity of a single interferometer[17,30].

The scanning stage of TMFPI is shown in fig. 3.1. The scanning mirrors of two interferometers are mounted on the same scanning stage to obtain both stationary and dynamically stable synchronization. The spacing of the two interferometers satisfies

$$d_2 = d_1 \cos\alpha \tag{3.7}$$

The first interferometer of spacing d_1 transmits wavelengths

$$\lambda_1 = \frac{2d_1}{m_1} \quad \text{for integral } m_1 \tag{3.8}$$

while the second interferometer of spacing d_2 transmits wavelengths

$$\lambda_2 = \frac{2d_2}{m_2} \text{ for integral } m_2 \tag{3.9}$$

Only if $\lambda_1 = \lambda_2$ will light be transmitted through the tandem combination. Therefore the FSR of the TMFRI is increased by about a factor of 20 over that of the single interferometer if offset angle α is 18°. Elimination of neighboring interference orders in a tandem arrangement is shown in fig. 3.2. Only ghosts of neighboring orders remain.

Fig. 3.1: A diagram of a translation stage designed to automatically synchronise the scans of two interferometers after Sandercock[30]. d_1 and d_2 are spacings of FP1 and FP2 respectively. α is the offset angle.

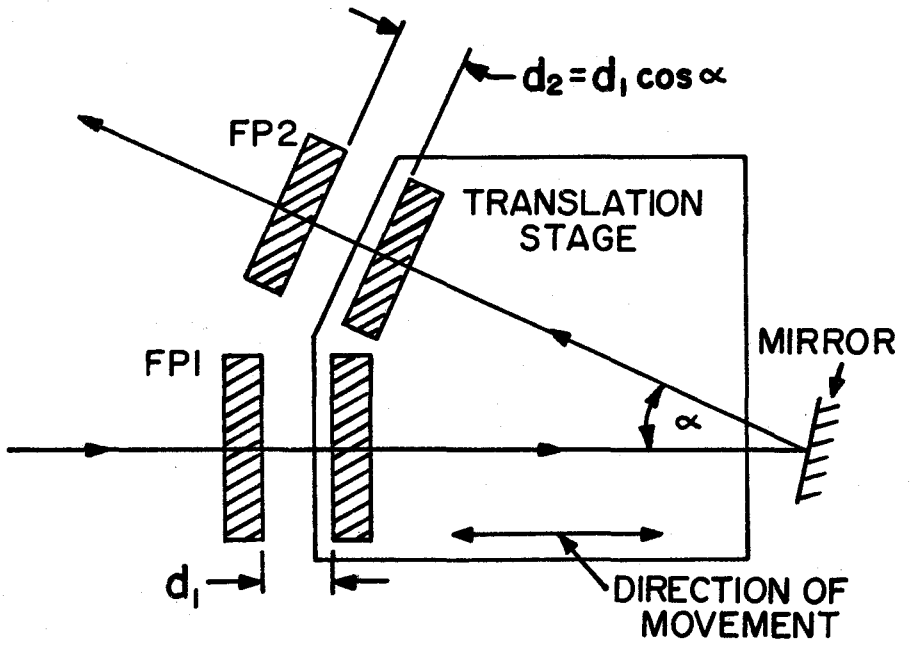
$d_2 = d_1 \cos \alpha$
FP2
TRANSLATION STAGE
MIRROR
FPI
α
d_1
DIRECTION OF MOVEMENT

Fig. 3.2: Scheme of elimination of neighboring interference orders in a tandem arrangement after Sandercock[30]. Only ghosts of neighboring orders remain.

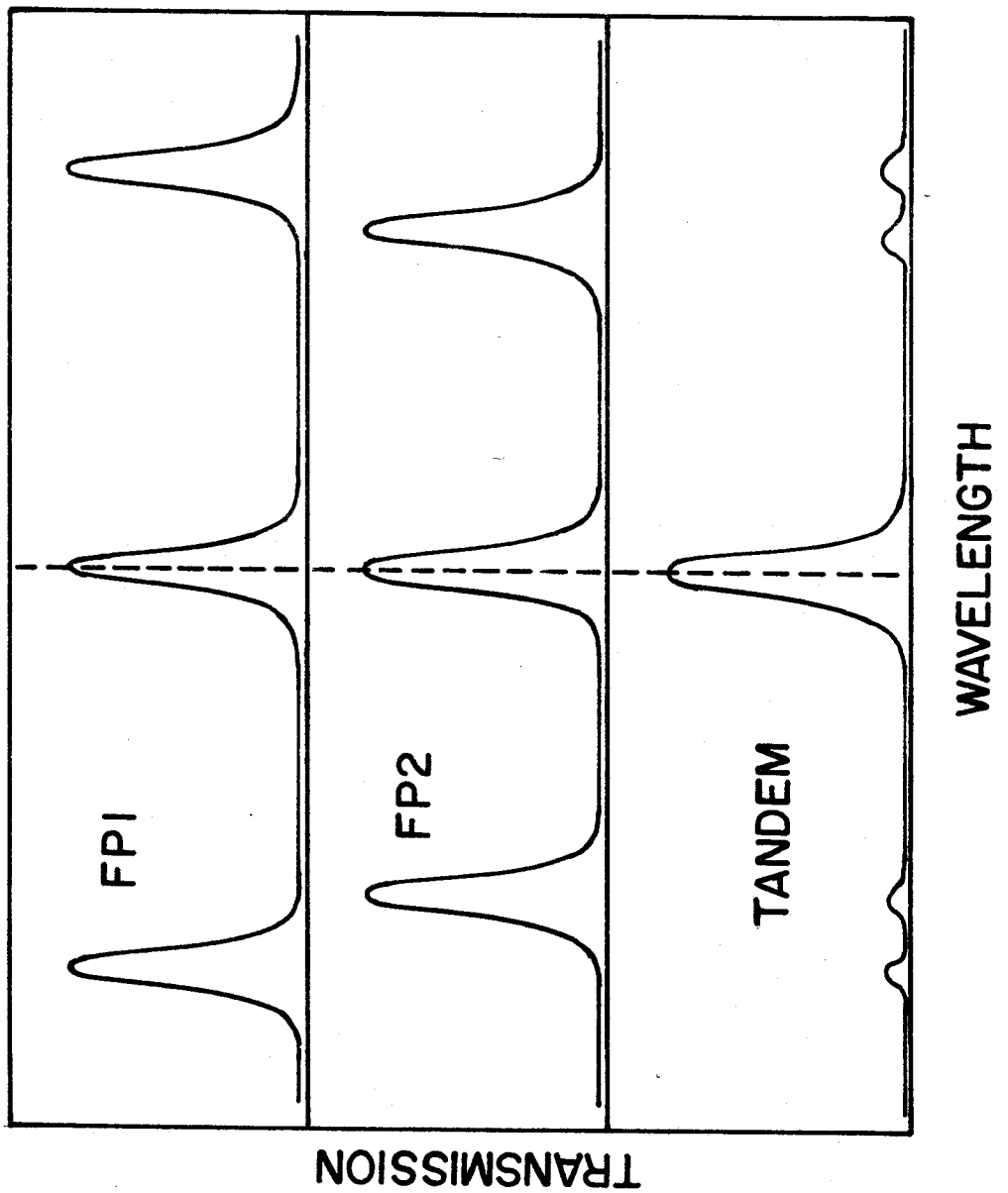
FP1
FP2
TANDEM
TRANSMISSION
WAVELENGTH

3.2 Experimental arrangement

A block diagram of the experimental apparatus is shown in fig. 3.3. The light source used is a Coherent Innova 90-3 Argon-Ion laser whose most intense emmission is at 5145 Å with an output power of 1400 mw in multi-modes. For these experiments which require a single mode with very narrow linewidth, the Coherent model 923 solid fused silica etalon was installed. The typical frequency drift of the etalon is about ± 20 MHz/0.01°C. After a 25-min warm up period, the output laser beam has an optical noise of 0.2% RMS, a frequency stability of ± 4 MHz/sec and an intensity stability ranging ± 0.5%.

The sample was mounted in a copper holder with the top surface contacting an indium anchor and the bottom surface contacting a copper-constantan thermocouple. A H.P. 3420B DC differential voltmeter with sensitivity 0.1 μv was used to measure the potential across the thermocouple, using liquid N_2 as a reference temperature.

To provide adjustable heating, a 300Ω, 0.5W resistor connected with a H.P. 6218A power supply was soldered to the sample holder. The sample and its holder were installed in an optical cryostat made by Sulfrian Cryogenics Inc. as shown in fig. 3.4. Chamber 1 holds about 2 litres of liquid helium (or nitrogen) which cools the specimen by thermal conduction through the bar (10). The specimen can be changed by opening the O-ring joint between (3) and (4) and the joint (15). The cryostat has three optical glass windows on three sides separated by 90° to permit both 90° and 180° scattering angles.

To prevent sample surface deterioration, the cryostat was pumped out to below 10^{-5} Torr with a diffusion pump and a liquid

Fig. 3.3: Block diagram of experimental arrangement.

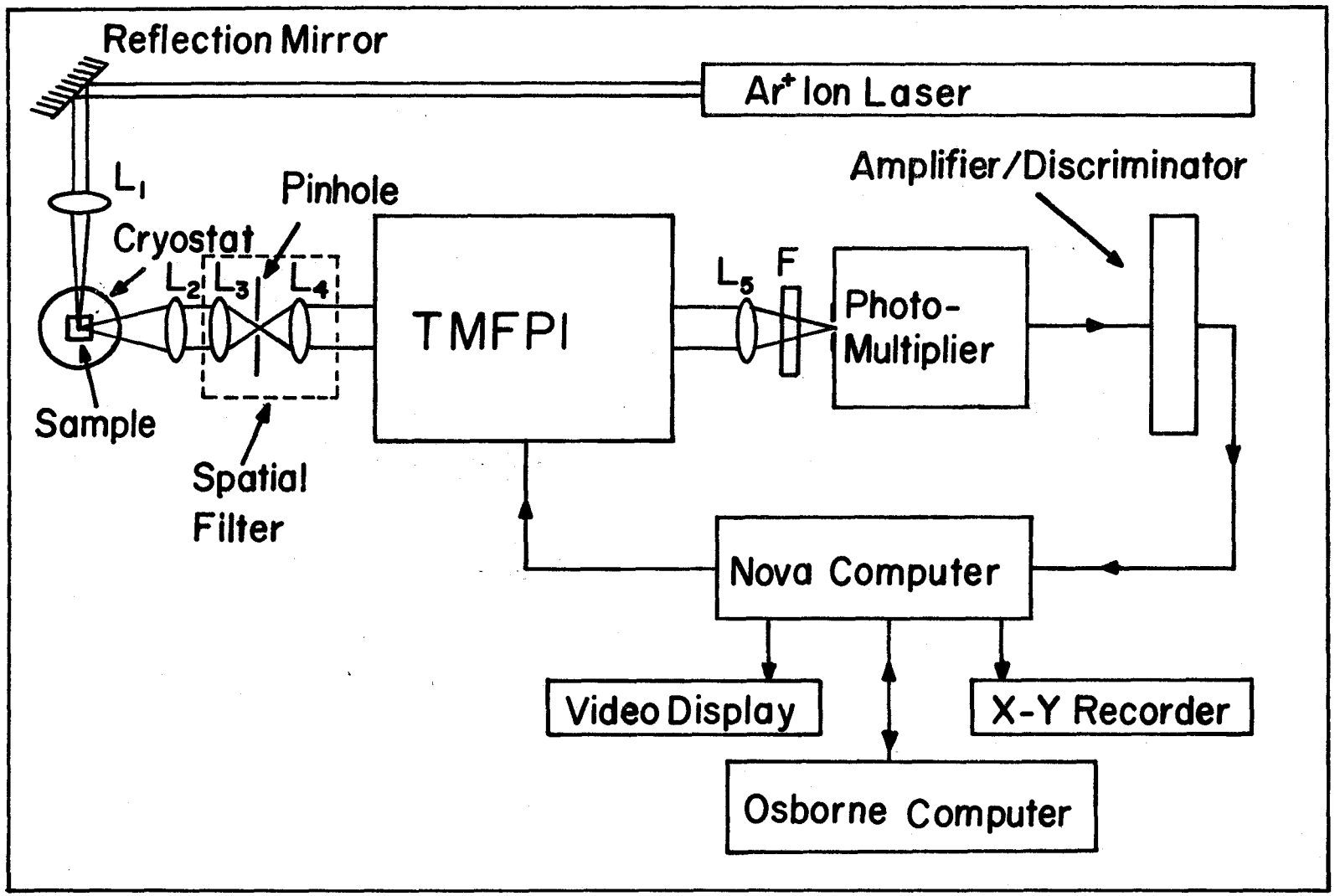
Reflection Mirror
Ar+ Ion Laser
L1
Pinhole
Amplifier/Discriminator
Cryostat
L2
L3
L4
TMFPI
L5
F
Photo-
Multiplier
Sample
Spatial
Filter
Nova Computer
Video Display
X-Y Recorder
Osborne Computer

Fig. 3.4: The optical cryostat diagram 1. Liquid He 2. Liquid N_2
3. Vacuum jacket 4. Vacuum shroud 5. Radiation shield
6. Window 7. Thermocouple 8. sample 9. heater resistor
10. thermoconducting bar 11. Helium pot 12. pumping valve
13. He exhaust vent 14. electric feedthrough 15. joint.

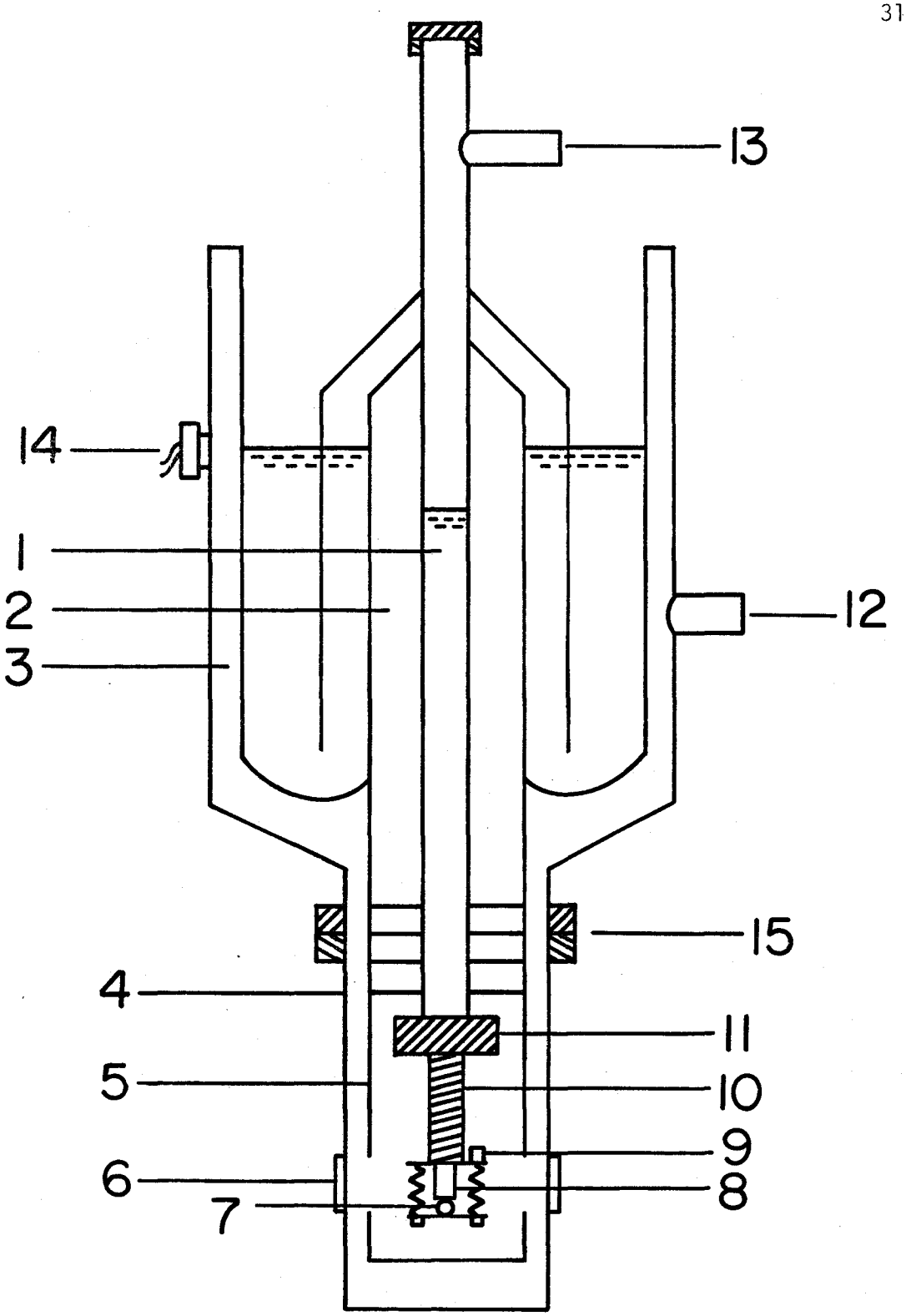
13
14
1
2
3
12
15
4
11
5
10
9
6
8
7

nitrogen trap backed by a mechanical roughing pump.

The roughing pump also was used to pump on the liquid nitrogen when it was necessary to obtain temperatures 1-15°K below that of liquid nitrogen (77.4°K). Usually the pumping speed was set so that a small amount of current through the control heater was required to hold the system at a given temperature for periods of time.

When very low temperatures were needed, liquid helium was transferred into the cryostat chamber from a storage dewar through a standard double-walled transfer tube after a precooling by liquid N_2.

The light collection system involves a focussing lens, L_1(f/5 cm), a collecting lens, L_2 (f/5 cm), and spatial filter consisting of two lenses, L_3(f/15 cm), L_4(f/10 cm), and a pinhole (100 micron). Each half of the tandem was operated in double pass for a total of four passes. The beam leaving the TMFPI was collected by a lens, L_5(f/30), passed through a band-pass filter F, and entered a photomultiplier. The filter was used to reduce the inelastically scattered light arising from fluorescence and the Raman scattering from the sample.

PMT Model FM130 made by the Electron Tube Division of ITT has a low dark current of 2×10^{-9} A at a gain of 5×10^{6}. The photomultiplier was installed in the TE-104 chamber (Products for Research Inc.) which provide water cooling for the tube without the requirement of supplemental cooling material such as dry ice. Cool-down time for the photocathode was 1 to 2 hours dependent on initial heat in the system. All of the optics described above are enclosed in a light tight box which helps reduce stray light, keeps the optics free of dust and minimizes the temperature variations in the enclosure.

After going through an Amplifier/Discriminator, MTN model 511, the signal was digitized with an A/D converter and its values stored in the memory of a 16-bit computer (Nova, Data General Co.). The computer also scanned the TMFPI and, via a D/A converter, provided feedback to the TMFPI to maintain mirror parallelism. Using a video interface, the spectrum was displayed on a TV monitor.

3.3 Sample preparation

The $(KBr)_{1-x}(KCN)_x$ mixed crystals were grown in the crystal growth lab of the University of Utah from zone-refined KBr and KCN. The CN^- concentrations were determined by chemical analysis with an error of 3%. Samples were cleaved along {100} planes with a razor blade and typically had dimensions of 0.5 cm x 0.5 cm x 0.5 cm. Scattering from a rough crystal surface produces extremely intense reflections which may overlap and mask the Brillouin components. So in these experiments, at least three "clean" surfaces are required for each sample. The cleaved samples were put under vacuum quickly so that the surfaces of the crystals would not deteriorate by exposure to moisture in the air.

3.4 Brillouin spectra measurement

In order to measure the spectra of T_{2g} phonons which propagate along [110]-direction and are polarized in [001]-direction, a 90° scattering geometry is used. The (100) surface of the sample was perpendicular to the incident beam and the (010) surface was perpendicular to the scattered light. The incident beam must be located near

the centre of the sample to prevent the strong surface scattering. By adjusting the dewar position, the light transmission through the crystal could be maximized to attenuate the surface reflections.

By carefully arranging lens L_1 and spatial filter, the incident laser is focussed on the crystal and scattered light is collimated and perpendicular to mirrors of TMFPI.

Alignment of the TMFPI is very crucial in these experiments. At first one used a weak laser beam as a reference signal and aligned a 2-pass single interferometer with a corner cube retroreflector; then the 1-pass tandem was aligned; and finally, the 2-pass tandem system. For each step one should see that a bright and symmetric circle regularly collapsed towards the center of the circle on the mirror as the TMFPI was scanned. Following the coarse screw adjustments, fine correction was made by adjusting 5 potentiometers which controlled parameters Xl, Y_1, X_2, Y_2 and Δz, where X_1, Y_1 and X_2, Y_2 were used to control parallelism of FP_1 and FP_2 respectively. Δz is synchronisation axis, i.e. an adjustment of Δz will allow FP_2 to transmit one of the orders transmitted by FP_1. Therefore Δz is most critical and more time is spent on stabilizing this axis.

After aligning the TMFPI the crystal was put in position and the spectrum should appear in a videodisplay. Then one should optimize the whole optical system and make Brillouin peak as big as possible. The desireable temperatures were obtained by adding liquid nitrogen (or helium) into the cryostat. Fixing the rate of pumping and laser output power, one can change the voltage of the heater to maintain the temperatures.

The dynamic stabilization of the alignment of the TMFPI was controlled by sending correcting voltages to the piezoelectric stacks from the computer-controlled D/A.

To improve counting efficiency in the low intensity Brillouin region, the scan rate was four times slower in the region of the Brillouin peaks than in the region of the Rayleigh peaks. Data of each scan were accumulated in the computer to get sufficient counts. At liquid N_2 temperature, collecting time was about 40 min. to obtain 1000 counts.

The very intense elastic scattering was attenuated by a "Rayleigh filter" which moved in when a Rayleigh peak came and moved out when a Brillouin peak came. Usually such filter is used in 180° scattering in which elastic peaks are much stronger than those in 90° scattering.

An Osborne computer which was interfaced to the Nova computer was used to store data and also to process deconvolution analysis.

3.5 Error Analysis

In this section experimental errors in Brillouin peak frequency and linewidth, as well as temperature meausrements will be discussed.

Experimental errors in Brillouin frequency measurement are primarily due to uncertainty of mirror spacing of the Fabry-Perot interferometer and statistical variation of the peak centre. A clock gauge attached to the interferometer provides the distance between the mirrors with an accuracy ±0.005 mm. For two typical free

spectral range, 3.505 GHz (d=42.82 mm) and 7.010 GHz (d=21.40 mm), errors are about ±0.004 GHz and ±0.002 GHz respectively. There may be an error in calibration of the clock gauge; however, it is a systematic error. After a warm-up period, the fluctuation in laser frequency is within 4 MHz. Therefore total error in phonon frequency measurements is rough 10 MHz.

Under conditions of constant laser output, the desired temperature was obtained by controling a heater and/or the pumping rate. The Copper-Constantan thermocouple was calibrated from 1.5K to 300K in units of microvolts. By setting the selection knob in the most sensible range, the differential voltmeter can be read within 0.1 μv which corresponded to ∿0.02K of deviation in temperature. In fact, because of the slow response of sample temperature to heat adjustments, the fluctuation in voltage was about ±1 μv at low temperatures and about ±8 μv at high temperatures, corresponding to an error of 0.6K around 20°K and an error of 0.3K around 77°K respectively.

A more serious error in temperature measurements comes from local laser heating. Because of the poor thermal conductivity of $(KBr)_{1-x}(KCN)_x$, there was a temperature gradient between the scattering volume and the sample surface which was in contact with the thermocouple. In order to decrease laser heating, one should make the laser power as low as practically possible. However, lowering laser power resulted in a decrease in the intensity of scattered light, it is necessary to compromise between the need to minimize local heating and have sufficient signal intensity. At 400 mw laser power, it was

estimated that there was a temperature difference of several degrees at very low temperatures and ∿1 degree around nitrogen temperature. Near room temperature, local heating can be neglected. The systematic error mainly arose from the calibration of the thermocouple.

For a reliable linewidth measurement, it is necessary to obtain sufficient counts in the Brillouin peak. According to the arguments of Walton et al.[36] a rule of thumb is that a difference in counts between the Brillouin peak and the Rayleigh peak, which is normalized to the Brillouin peak height, should be greater than the square root of the counts in the Brillouin line. In our experiments the counts for each Brillouin peak were over 1000 and satisfied the above criterion very well.

The linewidth is determined by fitting the Brillouin peak using the convolution of a Lorentzian function with the Rayleigh peak. From run to run, the finesse varied roughly from 46 to 50 so the linewidth measurements are accurate within ±15 MHz.

CHAPTER 4

RESULTS AND DISCUSSION

4.1 Anomalies in phonon frequency and linewidth

Brillouin spectra were taken using the 90°-scattering geometry described in chapter 3. The temperature dependence of the frequency of T_{2g} symmetry acoustic phonon is shown in Fig. 4.1 for several different CN^- concentrations of $(KBr)_{1-x}(KCN)_x$. The phonon frequency decreased as the crystals were cooled down until a freezing temperature T_f was reached; it increased on further cooling. When the CN^- concentration decreased, the shape of the frequency minimum broadened and the position of the minimum moved to lower temperature. The freezing temperature T_f is illustrated in Fig. 4.2 as a function of mole fraction of the cyanide ions and it decreased as CN^- concentration decreased.

These results are similar to the data taken by Satija et al.[31] The main difference is in the values of T_f at different concentrations. This may be due to: (1) position of the thermocouple, (2) different localized heating effects at different laser powers, and (3) fluctuation of the CN^- concentration of samples. The possible experimental error in frequency and temperature measurements are analyzed in chapter 3.

The full-width at half-maximum (FWHM) of the transverse phonon was obtained by convoluting a Lorentzian curve with the instrumental function and fitting this to the measured Brillouin line, using an

Fig. 4.1: The temperature dependence of the T_{2g} phonon frequency in $(KBr)_{1-x}(KCN)_x$ with x=0.20, 0.35 and 0.50. The solid circles describe the experimental data and the open circles arise from the theoretical calculation. Solid and dashed lines are guides to the eye.

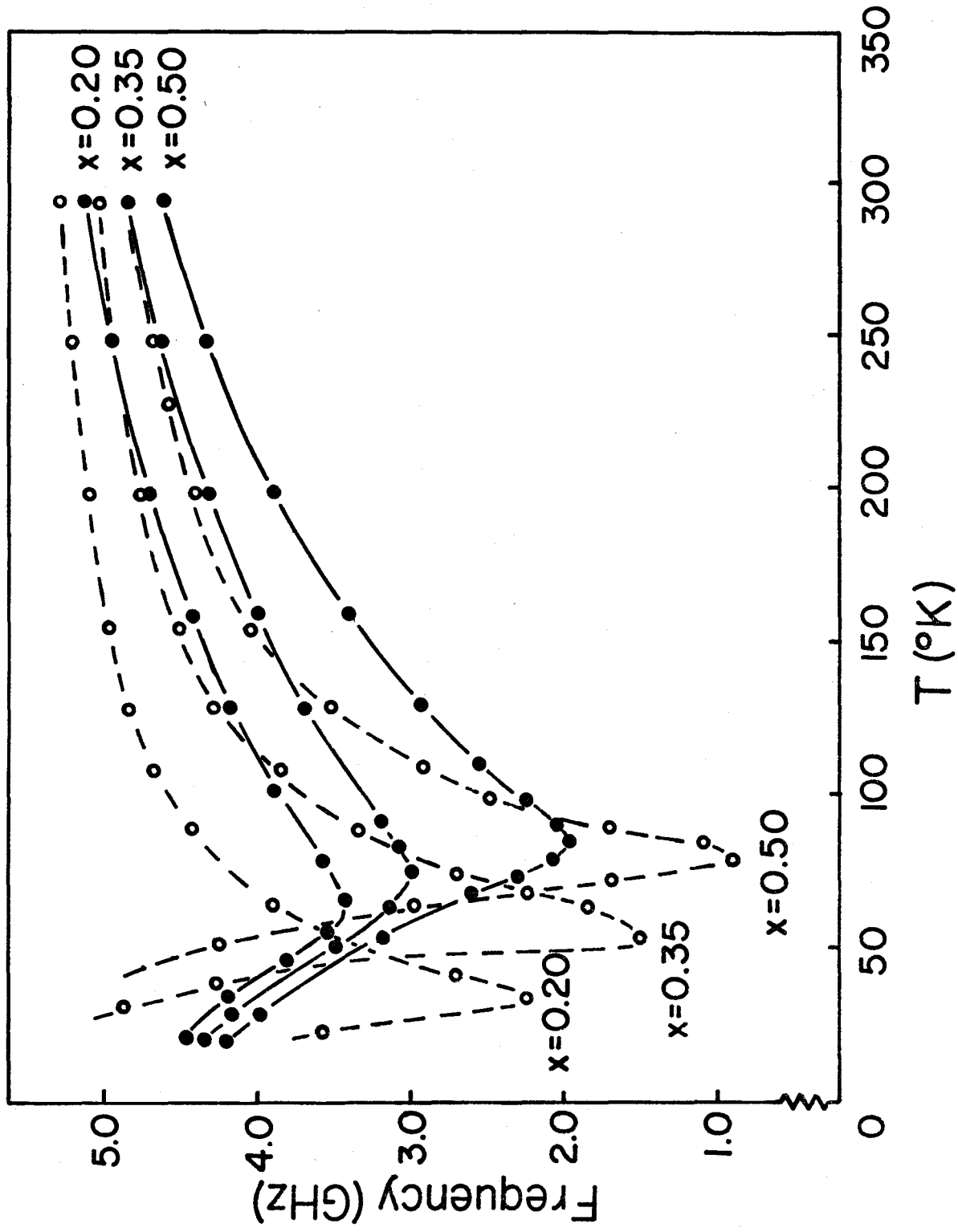
x=0.20
x=0.35
x=0.50
x=0.20
x=0.35
x=0.50
Frequency (GHz)
5.0
4.0
3.0
2.0
1.0
0
50
100
150
200
250
300
350
T (°K)

Fig. 4.2: Plot of the freezing temperature, T_f, versus CN^- concentration.

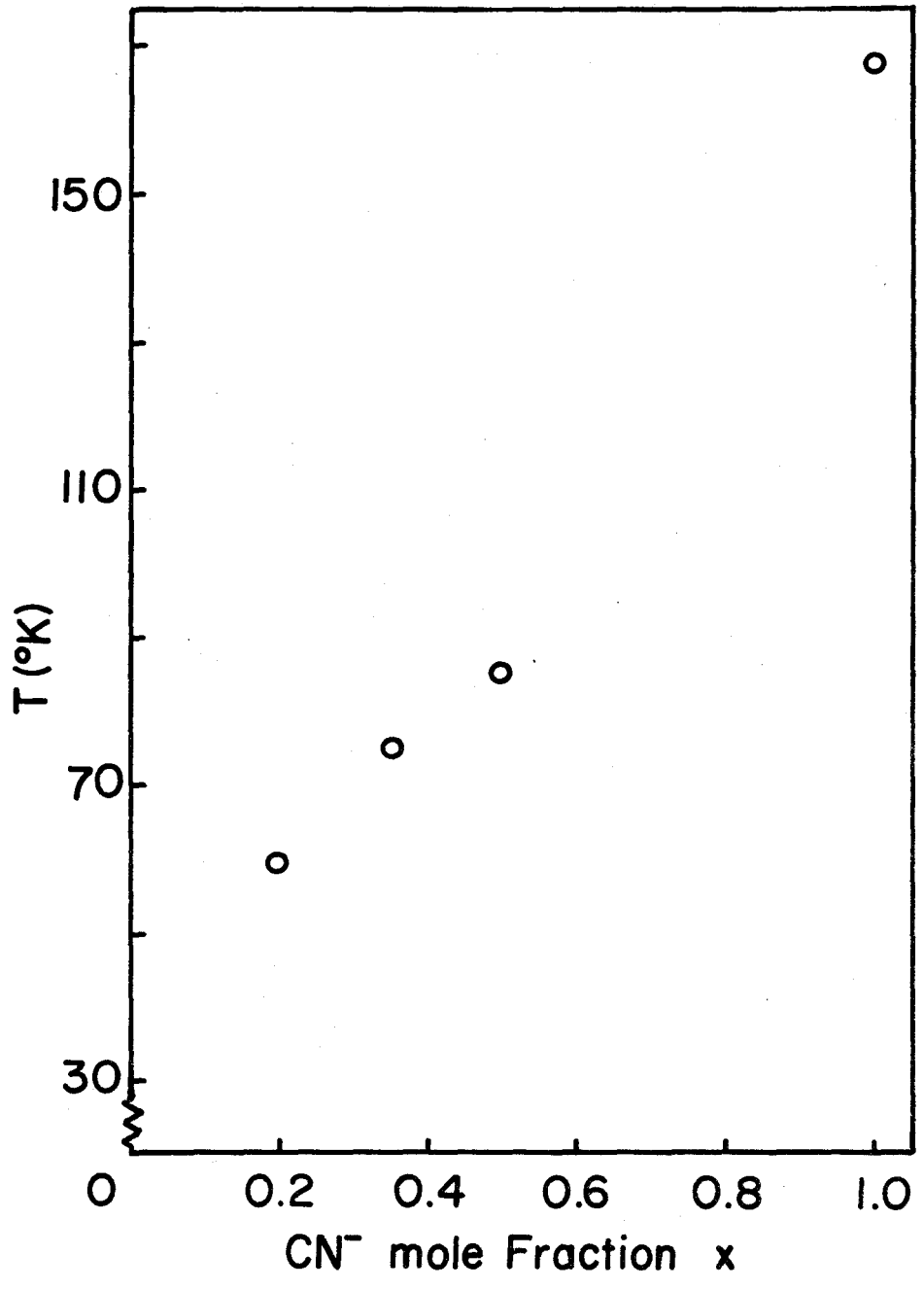
150
110
70
30
T (°K)
0
0.2
0.4
0.6
0.8
1.0
CN⁻ mole Fraction x

Fig. 4.3: The full width at half maximum of T_{2g} acoustic phonon for $(KBr)_{1-x}(KCN)_x$ with x=0.2 and 0.5, plotted as a function of the temperature. The dashed line is an interpolation between 85°K and 70°K (see text).

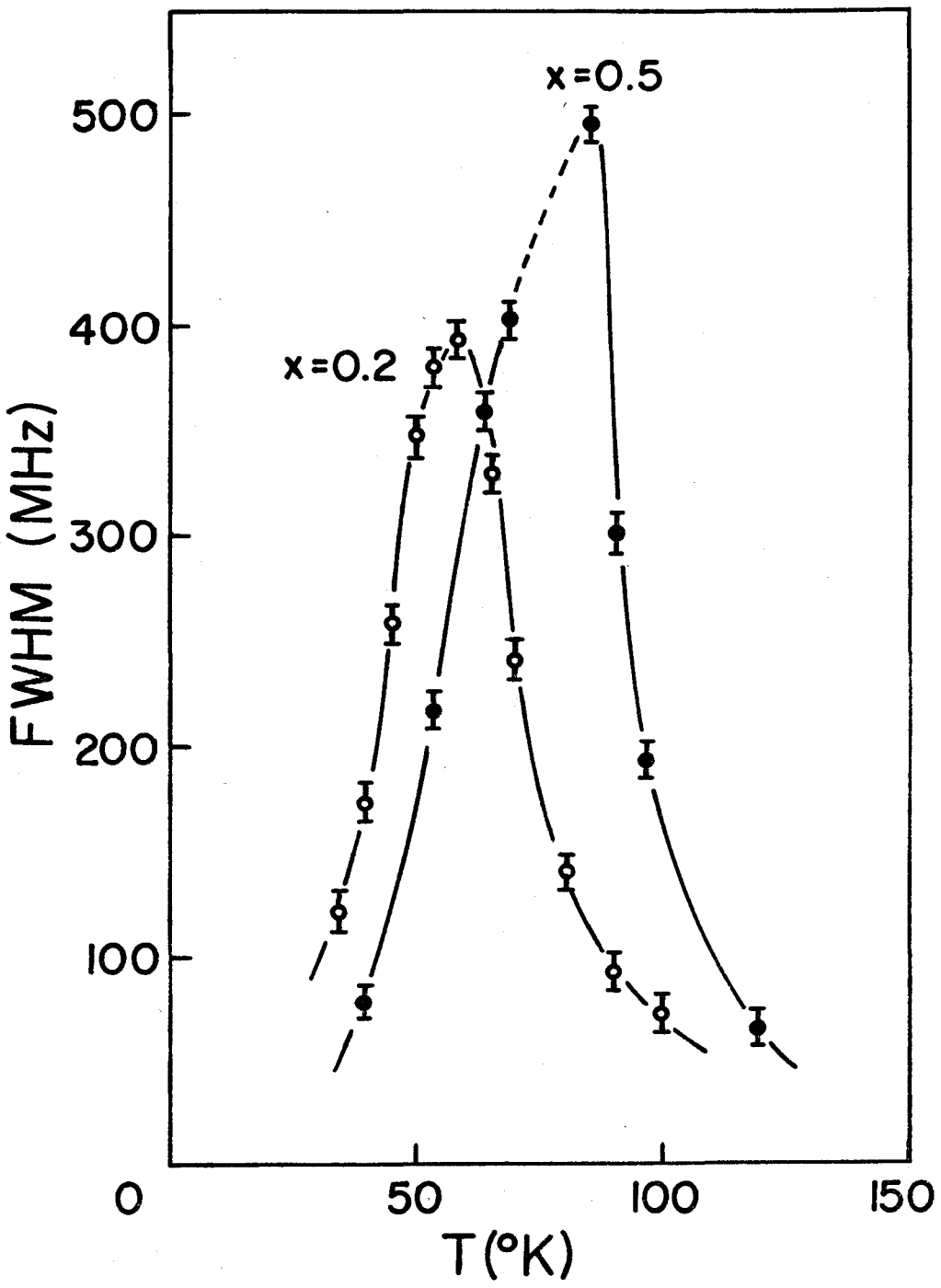
x=0.5
x=0.2
500
400
300
200
100
0
50
100
150
FWHM (MHz)
T(°K)

optimizing computer subprogram[32,34]. The results are plotted in Fig. 4.3 versus the temperature for CN^- mole fractions 0.20 and 0.50. As the temperature decreased from room temperature the linewidth increases until reaching a maximum value, marked by freezing temperature T_f. When the temperature decreased further the linewidth decreased. The freezing temperature is the same function of concentration as that of phonon frequency. It is noted that linewidth varied more dramatically than the frequency around the freezing temperature.

For x=0.5 and temperature ranging from 70K to 85K, there is a complex spectrum consisting of the phonon and multi-modes which will be examined later. Hence it is difficult to identify the linewidth in that region. FWHM was obtained by interpolation from data above and below the transition temperature.

It is interesting to compare experimental data taken by different probes which cover a very broad frequency range. These experiments include: dielectric[19] (87Hz-100kHZ), ultrasonic[10] (megahertz), neutron inelastic scattering[29] (terahertz), and Brillouin scattering (gigahertz) measurements. The freezing temperature is plotted in fig. 4.4 as a function of the logarithm of the measuring probe frequency at a concentration of 0.5. The solid circle points are taken from Loidl et al.[19], the square point from Garland et al.[10], the open circle point from Rowe et al.[29], and the open triangle data comes from our measurements. The sample in Garland's group has 49% CN^- and the samples in the other three groups are claimed to have 50% CN^-. There may be some fluctuations in the actual concentration, which would influence the accuracy of the comparison. There also is

Fig. 4.4: The frequency dependence of the freezing temperature, T_f, at x=0.5. The solid circle data are taken from Loidl et al.[19] the open circle point from Rowe et al.[29], the open square from Garland et al.[10], and the open triangle point from our measurements.

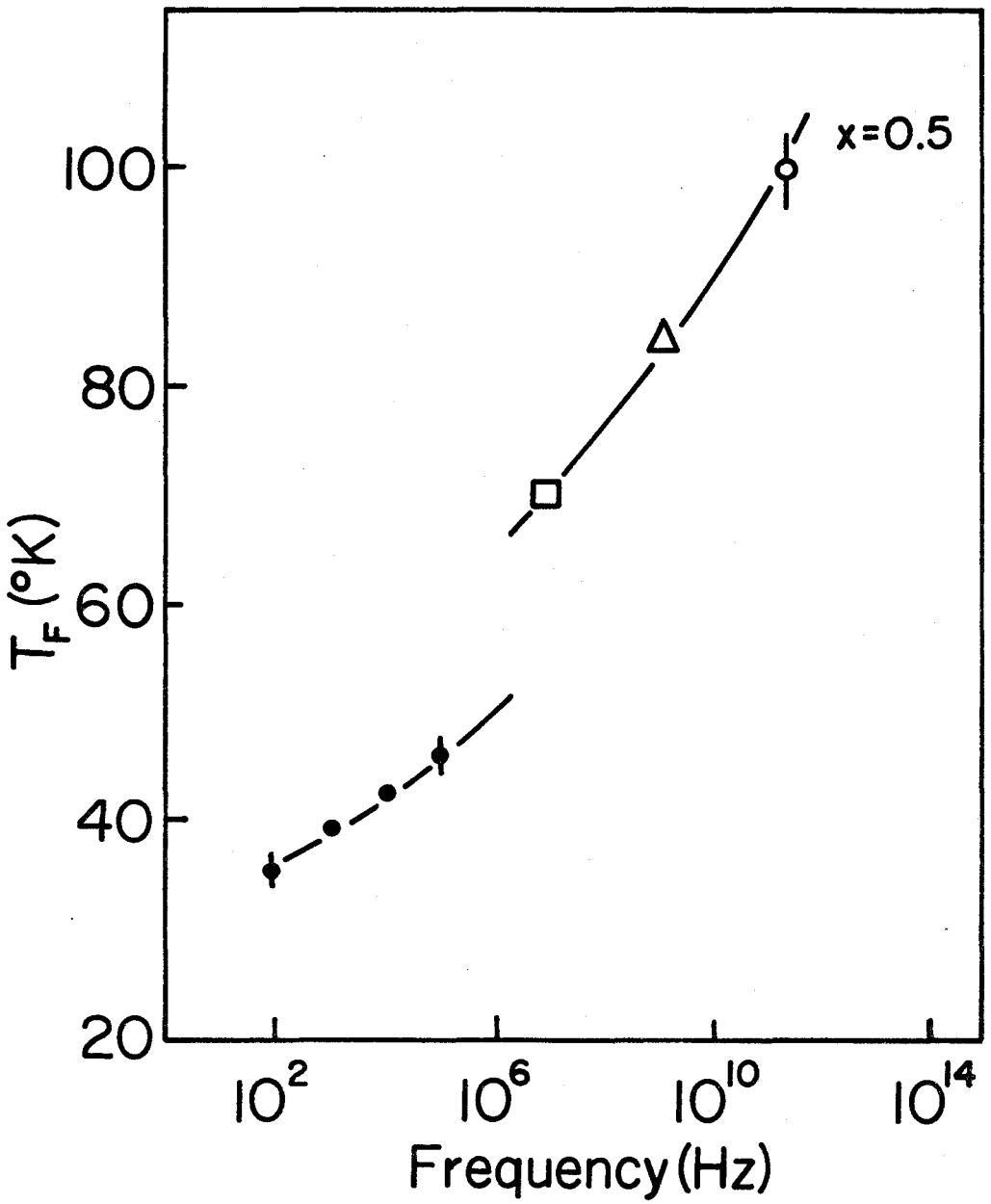
x=0.5
100
80
60
40
20
T_F (°K)
10^2
10^6
10^{10}
10^{14}
Frequency (Hz)

some question as to the validity of plotting the data in this way since the ultrasonic, Brillouin scattering and neutron scattering measurements probe the quadrupolar susceptibility (elastic reorientation)[4,23] while the dielectric measurements probe the electric dipolar susceptibility (electric reorientations)[19]. However, it is apparent that the freezing temperature is strongly frequency dependent and it moves to lower temperature with lower probe frequency.

4.2 Comparison with theory

Michel's theory developed in Chapter 2 will be compared with the experimental results in this section. At first we may present a theoretical calculation for the renormalized phonon frequency. By inserting eqs. (2.15), (2.16) and (2.17) into eq. (2.18), we immediately obtain the phonon frequency ω as a function of temperature and concentration. Some necessary parameters are given by Michel et al.[22] as follows:

The transverse phonon frequency ω_1 in pure kBr is 0.023 mev/$\hbar$ (or $\frac{\omega_1}{2\pi}$ = 5.6 GHz) which is determined by Brillouin scattering. Eigenvalue δ of the coupling matrix $\overleftrightarrow{C}$ equals to 1355.6°K following Michel et al.[22] In order to find Λ_∞ in eq. (2.10), we used the experimental data taken by the nuclear magnetic resonance technique[37] which gave λ, relaxation frequency of CN^- ions, a value of 0.28 $\frac{meV}{\hbar}$ (or $\frac{\lambda}{2\pi}$ = 68 GHz) at 100°K. The function y(T) defined in eq. (2.6) is quite complex. According to Michel et al.'s calculation, y increased continuously with decreasing temperature between 0.101 and 0.124 in the temperature interval 350 $\sim$ 54°K. Due to the change of y(T)

Table 1: Calculated values of parameters and phonon frequencies as a function of temperature for $(KBr)_{1-x}(KCN)_x$ with x=0.20.

T(°K)	y	$\Omega^2(\frac{meV}{\hbar})^2$ $x10^{-4}$	$\beta^2(\frac{meV}{\hbar})^2$ $x10^{-4}$	$\lambda(\frac{meV}{\hbar})$	ω(GHz)
300	0.104	4.79	0.497	0.97	5.29
250	0.106	4.68	0.608	0.80	5.23
230	0.107	4.62	0.609	0.72	5.19
200	0.109	4.51	0.781	0.62	5.13
154	0.111	4.23	1.06	0.46	4.98
130	0.113	4.04	1.25	0.39	4.87
110	0.118	3.75	1.54	0.31	4.69
101	0.1186	3.61	1.68	0.29	4.60
95	0.119	3.49	1.80	0.26	4.52
90	0.120	3.38	1.91	0.23	4.46
85	0.1204	3.26	2.03	0.21	4.38
80	0.121	3.12	2.17	0.19	4.29
75	0.1216	2.96	2.33	0.16	4.18
70	0.122	2.79	2.50	0.14	4.07

Table 1 continued

T(°K)	y	$\Omega^2(\frac{meV}{h})^2$ $x10^{-4}$	$\beta^2(\frac{meV}{h})^2$ $x10^{-4}$	$\lambda(\frac{meV}{h})$	ω(GHz)
65	0.1227	2.58	2.71	0.12	3.92
55	0.124	2.06	3.23	0.085	3.55
41.5	0.125	0.956	4.33	0.040	2.72
27.5	0.127	1.33	3.96	0.005	3.60

Table 2: Calculated values of parameters and phonon frequencies as a function of temperature for $(KBr)_{1-x}(KCN)_x$ with x=0.35.

T(°K)	y	$\Omega^2(\frac{meV}{\hbar})^2$ $x10^{-4}$	$\beta^2(\frac{meV}{\hbar})^2$ $x10^{-4}$	$\lambda(\frac{meV}{\hbar})$	ω(GHz)
300	0.104	4.42	0.870	0.97	5.08
250	0.106	4.23	1.06	0.80	4.97
230	0.107	4.12	1.17	0.72	4.91
200	0.109	3.92	1.38	0.62	4.79
154	0.11	3.43	1.86	0.46	4.49
130	0.113	3.10	2.18	0.39	4.27
110	0.118	2.60	2.69	0.31	3.91
101	0.1186	2.34	2.95	0.29	3.71
95	0.119	2.15	3.14	0.26	3.55
90	0.120	1.94	3.35	0.23	3.38
85	0.1204	1.73	3.56	0.21	3.20
80	0.121	1.49	3.79	0.19	2.97
75	0.1216	1.22	4.07	0.17	2.69
70	0.122	0.915	4.37	0.14	2.34
65	0.123	0.550	4.74	0.12	1.83

Table 2 continued

T(°K)	y	$\Omega^2(\frac{meV}{h})^2$ $x10^{-4}$	$\beta^2(\frac{meV}{h})^2$ $x10^{-4}$	$\lambda(\frac{meV}{h})$	ω(GHz)
55	0.124	0.369	5.66	0.085	1.53
41.5	0.1254	2.29	7.58	0.040	4.37
36	0.126	3.49	8.78	0.025	4.92

Table 3: Calculated values of parameters and phonon frequencies as a function of temperature for $(KBr)_{1-x}(KCN)_x$ with x=0.50.

T(°K)	y	$\Omega^2(\frac{meV}{\hbar})^2$ $x10^{-4}$	$\beta^2(\frac{meV}{\hbar})^2$ $x10^{-4}$	$\lambda(\frac{meV}{\hbar})$	ω(GHz)
300	0.104	4.05	1.24	0.97	4.86
250	0.106	3.77	1.52	0.80	4.70
230	0.107	3.62	1.67	0.72	4.60
200	0.109	3.34	1.95	0.62	4.42
154	0.111	2.64	2.65	0.46	3.93
130	0.113	2.17	3.12	0.39	3.57
110	0.118	1.44	3.85	0.31	2.91
101	0.1186	1.08	4.21	0.29	2.52
95	0.119	0.80	4.49	0.26	2.17
90	0.120	0.51	4.78	0.23	1.73
85	0.1204	0.21	5.08	0.21	1.12
80	0.121	0.13	5.42	0.19	0.89
75	0.1216	0.52	5.81	0.16	1.77
70	0.122	0.96	6.25	0.14	2.41
65	0.123	1.48	6.77	0.12	3.01
55	0.124	2.79	8.08	0.085	4.30

versus temperature being very small, for simplicity, values of y(T) are obtained by linearly interpolating the known data y(350°K) and y(54°K).

The calculated parameters and phonon frequency for concentrations 0.20, 0.35 and 0.50 are presented in table 1, 2, and 3 respectively. The phonon frequency versus temperature is also illustrated in open circles in Fig. 4.1. The dashed line is a guide to the eye. Theoretical phonon frequency curves have the same pattern as the experimental ones but they vary more rapidly around the freezing temperature. The minimum position is shifted to lower temperature. The lower the concentration, the worse the agreement with the experimental data.

Surprisingly if one uses theoretical parameters as fitting parameters, the phonon lineshapes obtained by theory and experiments agree very well. As shown in fig. 4.5, the solid line represents the phonon peak which is taken at 53.5°K with 50% CN^- sample and the dashed line represents the best fitting curve which is obtained by a calculation of a differential scattering cross section-related quantity $\Phi''(\omega)$ given in eq. (2.14) with fitting parameters Ω_1=1.30 x 10^{-2} mev/$\hbar$, β=4.18 x 10^{-3} mev/$\hbar$, and λ=0.01 mev/$\hbar$ which are quite different from the theoretical parameters Ω_1=1.75 x 10^{2} mev/h, β=2.90 x 10^{-2} mev/h, and λ=0.07 mev/h. This set of fitting parameters is closest to the theoretical set. The solutions of the best fit are not unique.

Although there is quantitatively a difference between the theory and experimental data, Michel's model may be used to qualitatively

Fig. 4.5: Comparison of two phonon peaks obtained by the Michel et al. theory with fitting parameters (dashed line) and from the experiment (solid line).

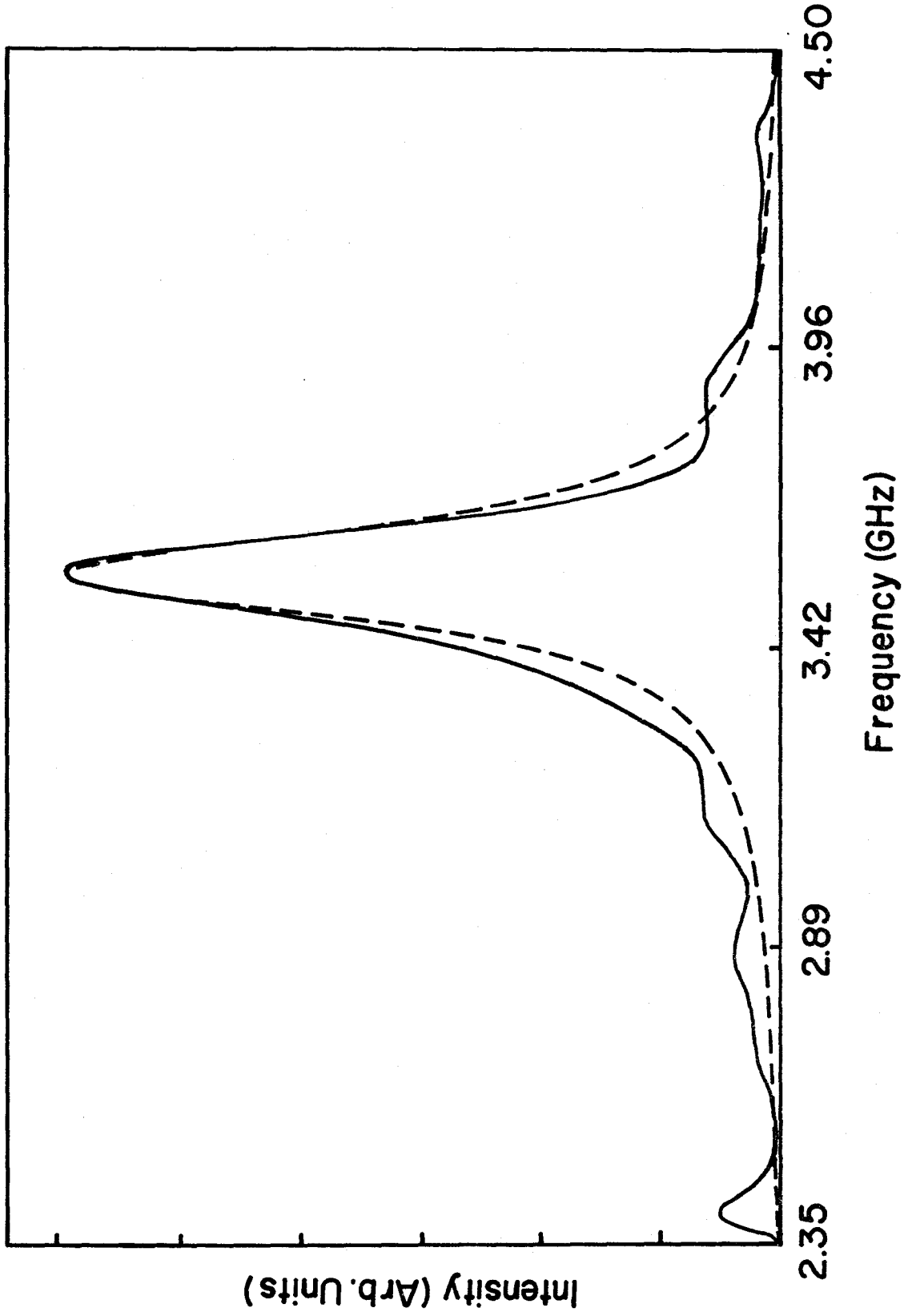
Intensity (Arb. Units)
2.35
2.89
3.42
3.96
4.50
Frequency (GHz)

explain the results as follows:

Near room temperature, the CN^- orientational relaxation is extremely fast compared with the phonon frequency. Hence the Brillouin peak is determined mainly by the "bare" phonon frequency ω_1. With a decrease in temperature, the relaxation frequency will decrease. When it becomes comparable to the phonon frequency, there is an increase in the coupling between the translational and orientational movements. Therefore the phonon undergoes soft-mode behavior. On further cooling, the system is able to reach the slow relaxation case, $\lambda_1 \leq \omega_1$. Orientational CN^- ions will not follow or respond to the phonon immediately and are gradually decoupled from the phonon. Hence the phonon frequency recovers from minimum values to the "bare" phonon frequency.

When the concentration of CN^- ions decreases, the average distance between the CN^- dipoles will increase. This results in a decrease in the effective interaction among the CN^- ions and therefore the freezing temperature decreases as the concentration decreases.

The inverse linewidth is proportional to the phonon lifetime when phonon-CN^- ion coupling increases, the phonon lifetime becomes shorter. Once the phonon is decoupled from the CN^- ions in the slow relaxation regime, its lifetime will increase. This is just what we observed in experiments. The theoretical phonon lifetime is decided by the imaginary part of the complex phonon frequency in Michel's theory and its value is not in agreement with the experimental results.

It is apparent that the freezing is not a static phenomenon, but a relaxational one. Depending upon the probe's frequency, the CN^- dipoles may or may not appear frozen. When CN^- ions could not follow probe any more, the system is referred to as frozen.

In these experiments, we did not see the central peak which supposedly appears at the freezing temperature and becomes stronger below T_f due to collective orientational relaxation. But we did observe an increase in the background just below the freezing temperature. It is possible that the extremely strong Rayleigh intensity masks the central peak, while the high background may arise from the tail of the central peak.

4.3 Observation of low-energy excitations

For the first time, we have observed new modes superimposed on the transverse phonon peak in KBr: KCN system. Their properties are examined in this section.

Fig. 4.6 shows a typical spectrum taken 8 hours after the sample with 0.5 CN^- concentration was cooled down to 80°K, which is 5K below its freezing temperature. Here the free spectral range was 3.505 GHz, laser output 400 mw at 5145 Å wavelength, and the collecting time 30 minutes. The phonon was located at 2.2 GHz and corresponded to the highest peak in the spectrum.

In order to obtain the "true" signal, the Bayesian deconvolution algorithm developed in chapter 2 was used. Inserting measured Brillouin peak M[x], Rayleigh peak R[x], and initial function $T^o[x]$

Fig. 4.6: Brillouin spectrum taken at 80K with a 3.505 GHz free spectral range. The sample was held at 80K for 6 hours before the data were collected. The collection time was 30 minutes.

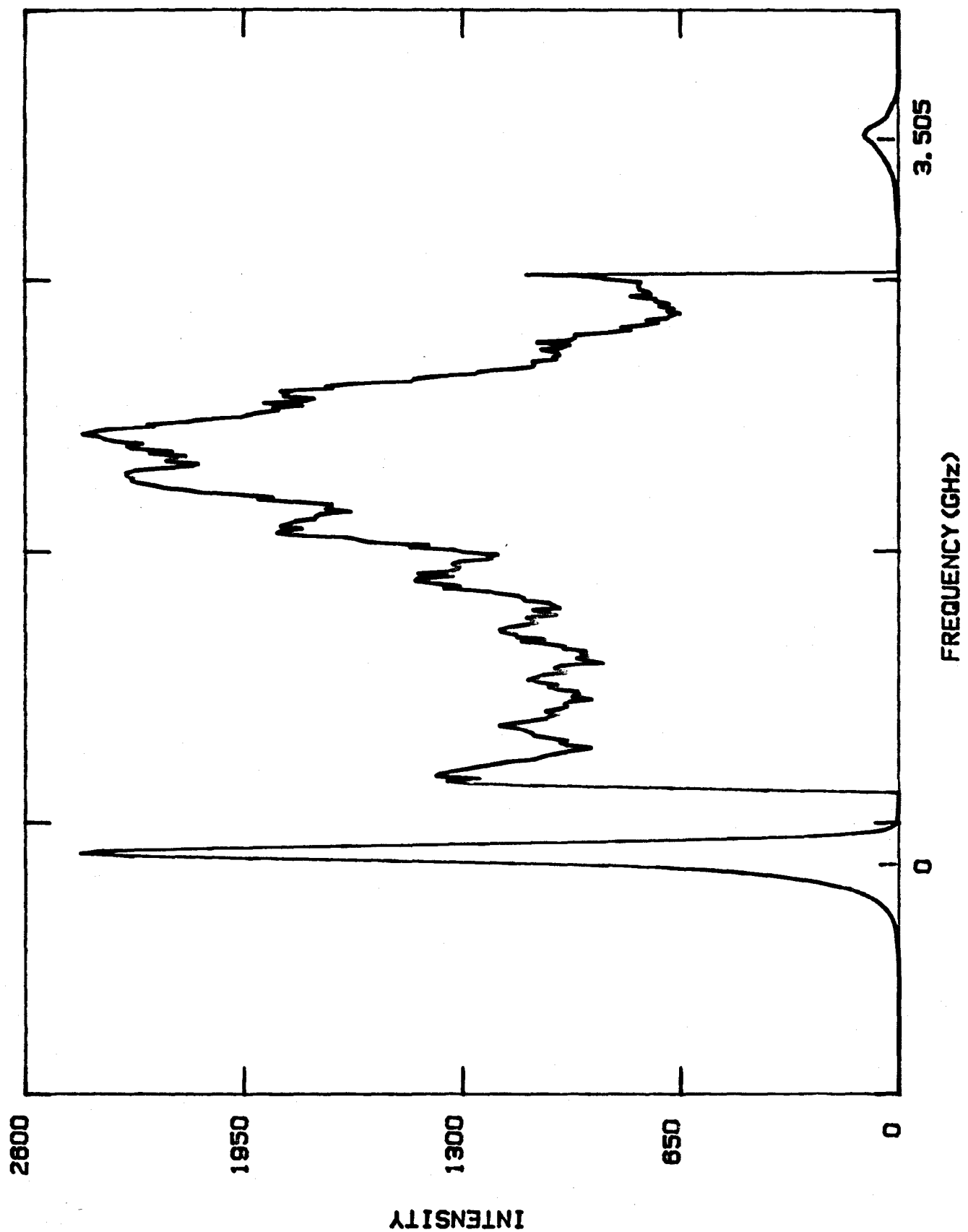
2800
1950
1300
650
0
INTENSITY
0
3.505
FREQUENCY (GHz)

Fig. 4.7: The result of deconvoluting the instrumental function from the spectrum in Fig. 4.6. The initial function is assumed to be a Lorentzian profile and the number of iteration cycles is 30.

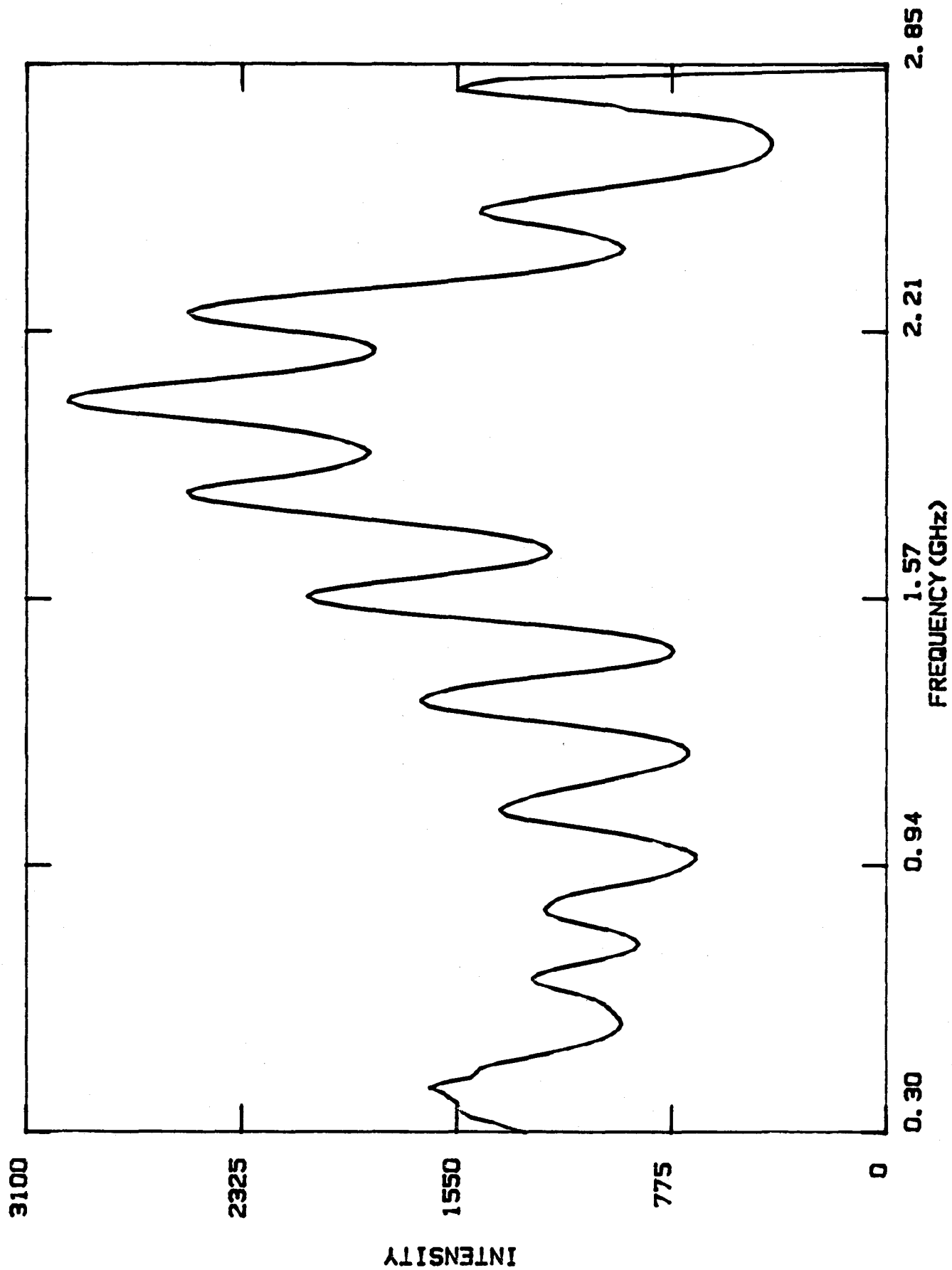
INTENSITY
3100
2325
1550
775
0
0.30
0.94
1.57
2.21
2.85
FREQUENCY (GHz)

which was assumed to be a Lorentzian profile, into eq. (2.43), we obtained a deconvoluted curve. The result after 30 iterations is shown in fig. 4.7. It is clear that the deconvolution algorithm greatly enhances the fine structure in spectrum, permitting easy identification of the mixed components.

The new modes are strongly temperature dependent. Above freezing temperature, no fine structure has been observed. The most distinct multi-modes usually occur at 5°K below the freezing temperature. This property clearly manifests that the new modes have nothing to do with either misaligning the Fabry-Perot interferometer or some other experimental artifact.

It takes a long time for these modes to develop. A sequence of spectra versus time is illustrated in the top curves in fig. 4.8. They are collected at different times after a 50% CN^- sample reaches 80°K from above T_f. Each spectrum is deconvoluted with the instrumental function and the results are presented in the bottom curves in fig. 4.8. Initially, the modes are hardly identifiable; as time goes on they become more and more distinct. The time to reach equilibrium becomes longer at lower temperatures, until it becomes impossible to wait long enough to obtain well-developed modes if the crystal is initially cooled from above T_f to temperature at about 15K below T_f.

The amplitude of the modes decreased with decreasing CN concentration. A series of deconvoluted spectra at temperatures 5K below T_f as a function of CN^- concentration is illustrated in fig. 4.9. At x=0.5 they appear very clear; as concentration decreases, they become less distinct and only show some little shoulders in the

Fig. 4.8: A sequence of three spectra taken at different times after reaching 80K. The bottom curves are the result of deconvoluting data as shown above each curve, the zero level has been changed for the deconvoluted data.

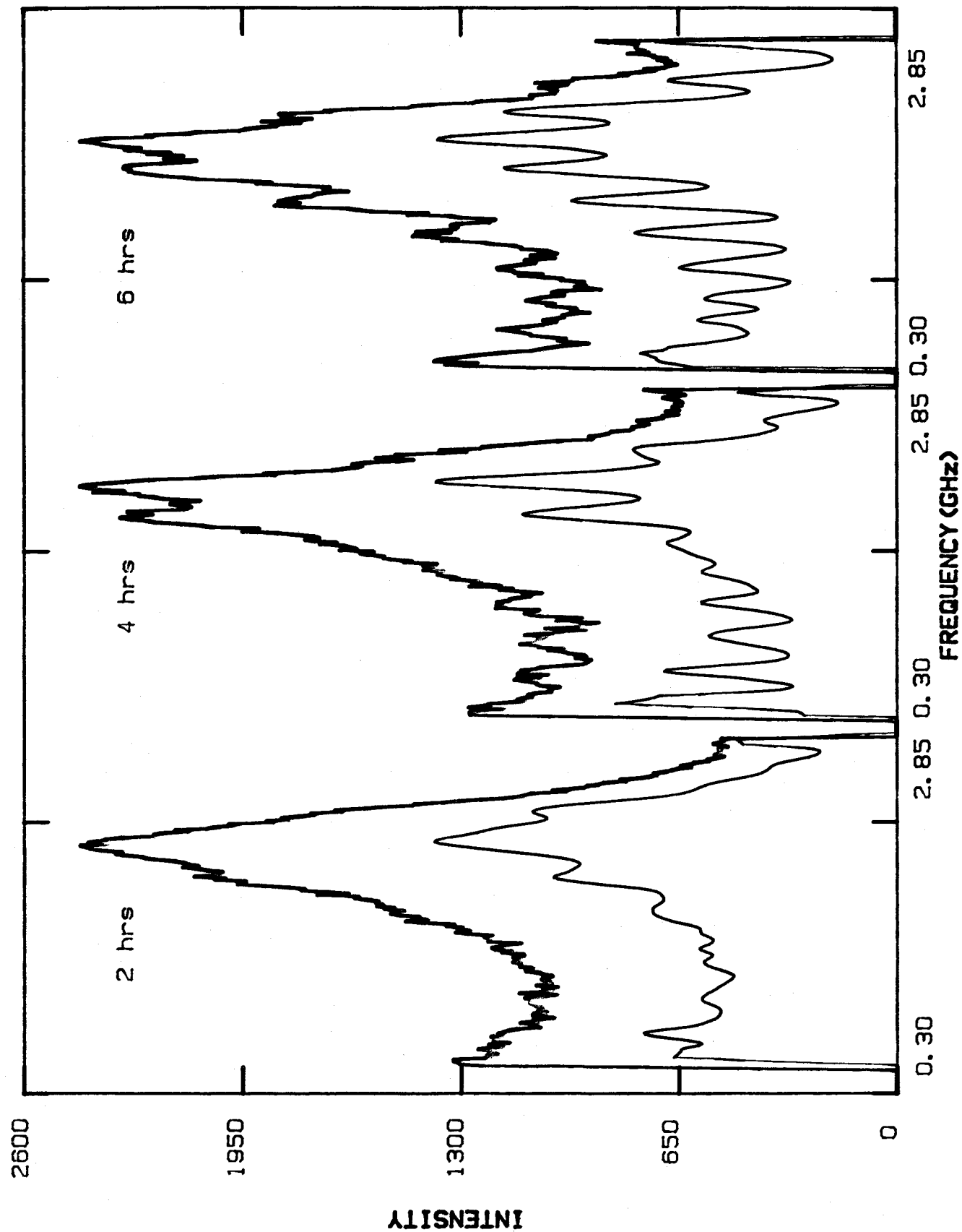
2 hrs
4 hrs
6 hrs
INTENSITY
2600
1950
1300
650
0
0.30
2.85
0.30
2.85
0.30
2.85
FREQUENCY (GHz)

Fig. 4.9: A series of phonon peaks at a temperature 5K below T_f as a function of CN^- concentration.

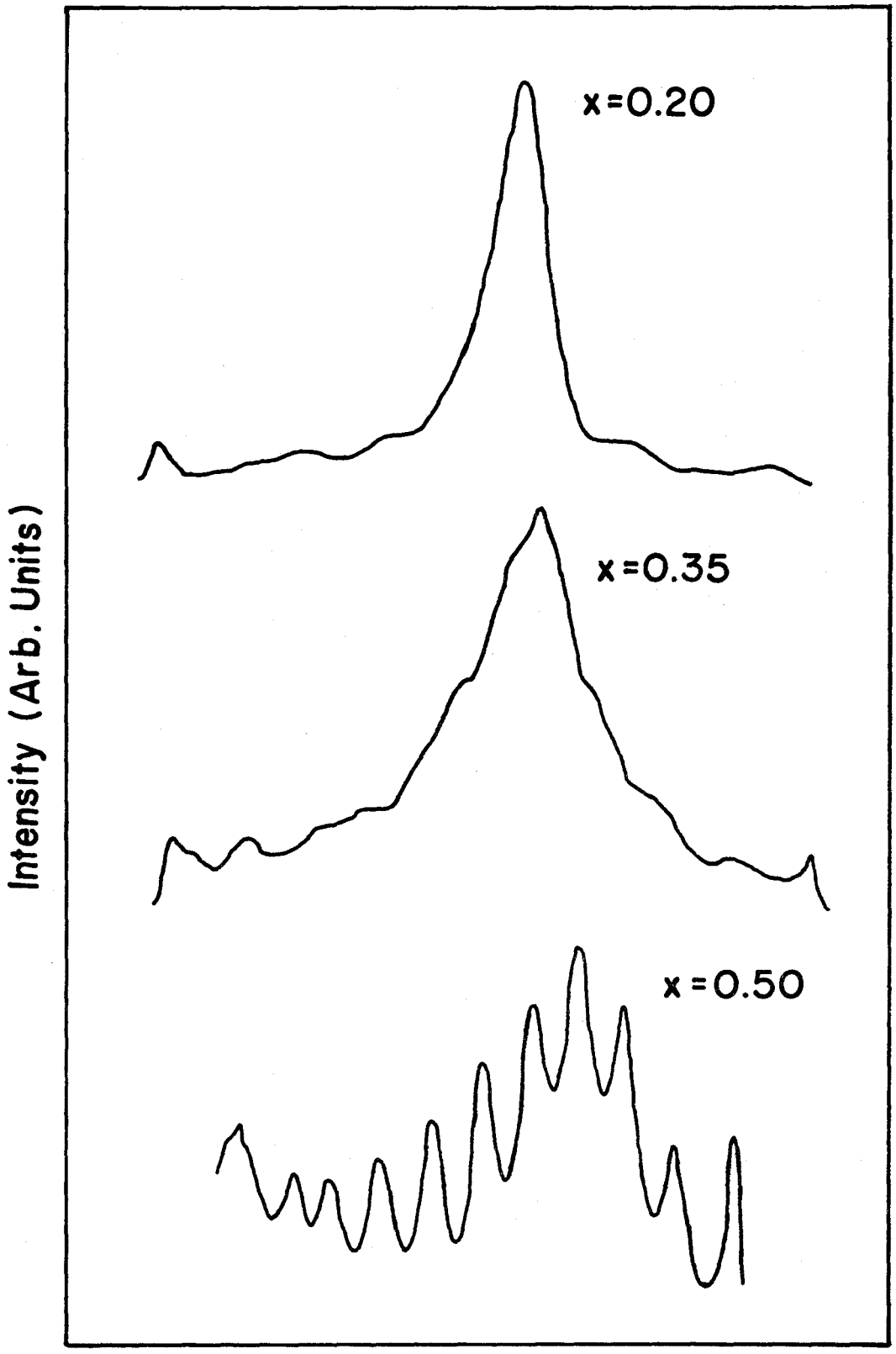
x=0.20
x=0.35
x=0.50
Intensity (Arb. Units)
Line Shape

Fig. 4.10: The ratio of the background on the low frequency side of the Brillouin peak, B, to the intensity of the Brillouin peak itself, I, at a temperature 5K below T_f as a function of CN^- concentrations.

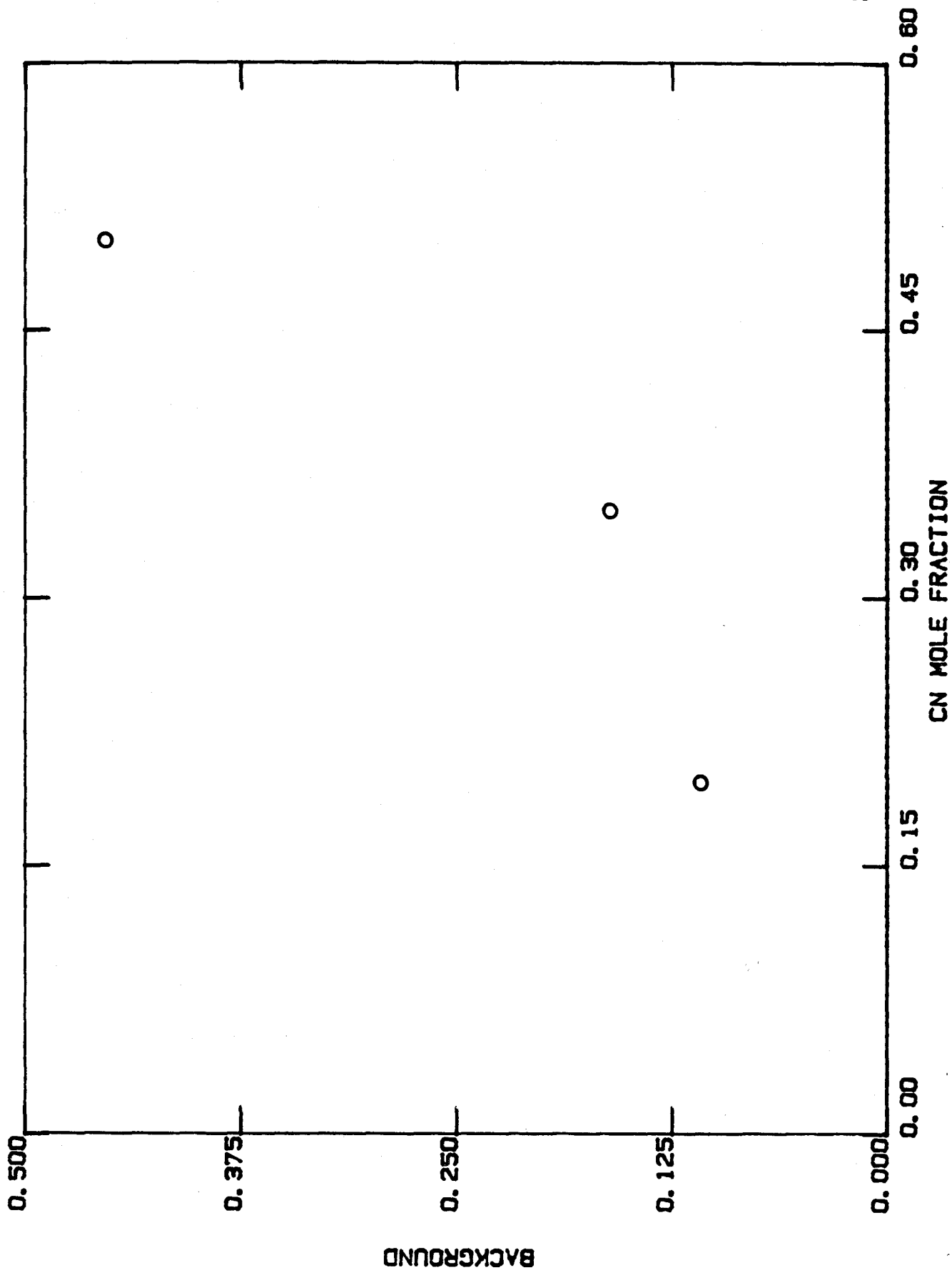
BACKGROUND
0.500
0.375
0.250
0.125
0.000
0.00
0.15
0.30
0.45
0.60
CN MOLE FRACTION

Fig. 4.11: Deconvolution curve for the Brillouin spectrum taken at 75°K with FSR=5.00 GHz was plotted as a solid line. Lorentzian fitting curve plotted as a dashed line consists of the phonon peak and the multi-modes.

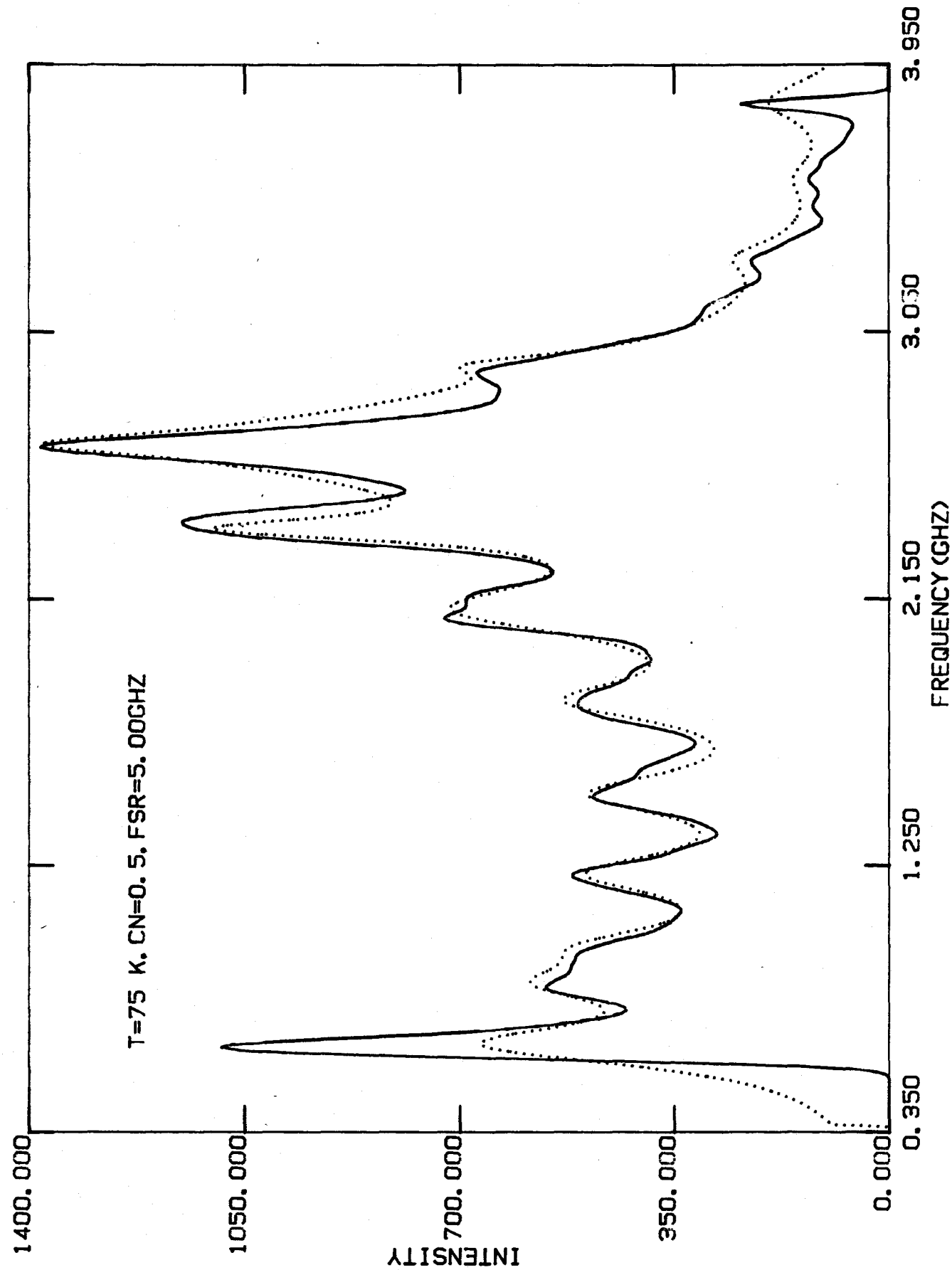
T=75 K, CN=0.5, FSR=5.00GHZ
INTENSITY
1400.000
1050.000
700.000
350.000
0.000
0.350
1.250
2.150
3.030
3.950
FREQUENCY (GHZ)

Table 4: Lorentzian fitting parameters for the deconvolution curve of Brillouin peak taken at 70°K with x=0.5 and free spectral range 5.00 GHz. The phonon is located at 2.64 GHz.

Height (arb. unit)	400	250	200	250	250	250	350	420	250	150	70	40	100	700
Width (MHz)	180	180	180	180	180	180	224	99	90	90	143	180	180	493
Position (GHz)	0.62	0.83	0.95	1.19	1.46	1.78	2.08	2.35	2.64	2.91	3.27	3.54	3.79	2.64

phonon peak at x=0.20. The concentration-dependent amplitude may be roughly estimated from the change in background. Considering different spectral intensities at different concentration, the background B should be normalized to the intensity of the phonon peak I. The ratio, B/I, is plotted in fig. 4.10 for a temperature 5°K below T_f, as a function of CN^- concentration.

New modes have an average spacing of 250 MHz in the 0.5 CN^- sample and their number appears to be roughly equal to the number of nearest neighbour CN^- ions. Fig. 4.11 shows the typical spectrum as a solid line which is the deconvolution curve of experimental data taken at 75°K with x=0.5 and free spectral range 5.00 GHz. The dashed line is the best-fitting curve which consists of Lorentzian-shaped modes and a Lorentzian-shaped phonon peak. The fitting parameters are listed in table 4.

4.4.A Possible explanation

It is well-known that the introduction of substitutional defects into crystals will modify the spectrum of the elementary excitation. Of course, for different systems, the physical origin of the modification is different. Two examples are given as follows:

MnF_2 is known as an antiferromagnetic material and has basic excitations — antiferromagnetic magnons. However in MnF_2:ZnF_2 mixed system, there are extra-modes which arise from the change in anisotropy field due to some of the nearest neighbours of a magnetic ion Mn^{++} being replaced with non-magnetic defect Z_n^{++} ion[5,35].

In solid methane there are tunneling excitations caused by the overlap of CH_4 wave functions in adjacent wells of a rotational potential. If deuterated methane is doped in the CH_4 crystal, similar multi-modes will be observed[28] due to the random replacement of nearest neighbours with molecules of different mass, CD_4, the tunnel splitting of CH_4 having thereby been changed.

Analogous to the above systems, it may be suggested that new modes in KBr:KCN alloy arise from the modification of tunneling levels due to interaction among CN^- dipoles. This modification will severely influence the coupling mode of phonon-CN^- defects.

As mentioned in chapter 2, the CN^- ion lies along <111>-directions in the octahedral potential of the KBr crystal. By quantum mechanical tunneling, the ground state of CN^- ion will split. Following Hetzler and Walton[12] the tunnel splitting may be written

$$n = 6*C^{3/2}*\exp(-C) \tag{4.1}$$

where C is a dimensionless parameter proportional to the square root of the height of the tunneling barrier, V, multiplied by the distance between the potential well, X_o. i.e.

$$C\alpha\ \sqrt{V}*X_o \tag{4.2}$$

The tunnel splitting, n is measured in k.

When CN^- concentration increases, the elastic interaction between CN^- ions becomes significant. The interaction energy for a nearest neighbouring CN^- pair is calculated in Chapter 2 and turns out to be about 5K. Of course this value is an approximation due to

the reasons given before. There is another method to estimate the interaction energy:

Pure KCN crystals undergo the first order transition from a cubic structure to a monoclinic structure at 168K due to the interaction between the CN^- ions. The contribution to this energy from the nearest neighbours may be obtained by dividing 168K by the Madelung constant for a face centred cubic lattice, 1.75; and is 96K. There are 12 nearest neighbours so the interaction energy between a pair of nearest neighbours would be 8K, which is close to the value obtained by Nowick et al. theory.

Considering the CN^--CN^- interaction, the potential in which the CN^- ion finds itself consists of three contributions: (1) the intrinsic barrier for an isolated ion, (2) the contribution from the nearest neighbours, and (3) the contribution from the next nearest neighbours and the rest of the crystal. The first is provided by the crystal field of the host lattice and is taken to be 24K[2], the second arises from the CN^- elastic dipole interaction and lies between 5K and 8K for each nearest neighbour site occupied by a CN^- ion. The third is estimated by the transition temperature for pure KCN, dividing by the Madelung constant and multiplying by 0.75, and the concentration of CN^-. Here it is assumed that the crystal beyond the nearest neighbours contributes 0.75, and the nearest neighbours 1, to the Madelung constant for a total of 1.75. The difference between the elastic constants of KBr and KCN is being ignored.

The largest tunnel splitting will be for an ion with no nearest neighbour sites occupied. The contribution to the "true"

potential beyond the nearest neighbours is 36°K for 0.5 CN^- concentration. Therefore the parameter C becomes

$$C = C_o \sqrt{\frac{36+24}{24}} = 1.6 * C_o \qquad (4.3)$$

where C_o is the value of C in the dilute crystal which will yield the observed[12] value of n=0.62K for non-interaction between CN^- ions.

Inserting this value for C in eq. 4.1 yields a maximum splitting of 0.3K, which is in agreement with the observed maximum of 0.2K, considering the approximations made.

The maximum splitting will decrease with CN^- ions occupying the nearest neighbours sites. The minimum splitting occurs if all the nearest neighbour sites are occupied, which is observed to be about 0.02K. There are two possibilities to explain the shape of the spectra: (1) new modes come directly from light which is scattered by different modified tunnel split ground states of the CN^- ions. The intensity is enhanced by the amplitude of the phonon peak. (2) modes arise from light scattered by the phonon component of a phonon-defect mixed mode. i.e. at first the phonon is coupled with different modified tunnel levels then it interacts with the photon.

Now we use the second possibility to explain time and temperature-dependence of the new modes. From chapter 2, we know that the frequency of CN^- reorientation decreases with decreasing temperature. When this frequency becomes less than that of the probe

(in this case the phonon) the system is referred to as "frozen" which is marked by a freezing temperature T_f. Above T_f the defects reorient faster than the phonon frequency, and any structure in the defect states cannot be seen. Just below T_f, the defects may be considered static and strongly couple with the phonon. Hence the phonon reveals the tunnel splitting. Below T_f, it takes a longer time for the CN^- ions which tend to occupy a lower energy configuration, to reorient. Thus the most easily identifiable spectra only begin to appear after about one hour 5K below the transition temperature and never appear at all at temperatures lower than about 15K below T_f due to the very long reorientational time required.

Finally the new modes are used to explain low temperature thermal properties in $(KBr)_{1-x}(KCN)_x$ which is similar to those in glasses.

The experiments[8] reveal: for $x<0.01$ the thermal conductivity is strongly reduced from that of pure KBr; however, as x increases beyond 0.01 the conductivity increases and has a behavior like PMMA. This indicates a disappearance of the individual CN^- tunneling states. In our model the interaction between CN^- ions in the nearest neighbours will increase the potential barrier, which results in an increased difficulty for CN^- ion tunneling and consequently, a decrease of the tunnel splitting.

The spacing of these modes is uniform resulting in the uniform density of states, which is characteristic of glasses.

CHAPTER 5

CONCLUSION

Anomalies in the transverse acoustic phonon in $(KBr)_{1-x}(KCN)_x$ alloy as a function of temperature with $0.2 \leq x \leq 0.5$ have been revealed by Brillouin scattering. For a given concentration the phonon frequency dips to a minimum while its linewidth reaches a maximum at a characteristic temperature T_f which is marked by the beginning of the formation of the orientational glass state in $(KBr)_{1-x}(KCN)$. T_f is strongly frequency and concentration dependent. It decreases with decreasing probe frequency and/or CN^- concentration. The anomalies are qualitatively explained by translational-orientational coupling proposed by Michel et al. However a quantitatively calculation of the phonon frequency is not in agreement with experimental data. Phonon lineshapes are well reproduced by the theory with three fitting parameters. It should be noted that these parameters are not unique.

We have observed new low-energy modes which are superimposed on the phonon peak at temperatures below the freezing temperature. These modes have an average spacing of 250 MHz in the 0.5 CN^- sample. Their number appears to be roughly equal to the number of nearest neighbour CN^- ions and their amplitude decreases with decreasing concentration. It takes about 1 hr for these modes to develop after cooling down from above T_f. Once the sample is raised above T_f, the fine structure will disappear.

A possible explanation suggested the initial tunneling level of CN^- are modified by interaction between CN^- dipoles. The interaction energy for two elastic dipole in nearest neighbouring is calculated about 5°K based on Nowick's et al. theory. This interaction will increase the tunneling barrier and hence decrease the tunneling levels. Different occupation of nearest neighbour sites corresponds to different splitting. Below T_f, the phonon can couple to the defect states, hence revealing the tunneling splitting.

Considering new modes are CN^--CN^- interaction dependent, a new experiment is suggested. By applying hydrostatic pressure or the external stress to the crystal, the interatomic distance will reduce and result in the increase of the interaction between CN^--CN^- dipoles. This may influence the separation of the modes and intensity.

BIBLIOGRAPHY

1. P.W. Anderson, B.I. Halperin and C.M. Varma, Phil. Mag. 25, 1 (1972).
2. A.U. Beyeler, Phys. Rev. B11, 3078 (1975).
3. S. Bhattacharya, S.R. Nagel, L. Fleishman and S. Susman, Phys. Rev. Lett. 48, 1267 (1982).
4. N.O. Birge, Y.H. Jeony, S.R. Nagel, S. Bhattacharya and S. Susman, Phys. Rev. B 30, 2306 (1984).
5. W.J.L. Buyers, D.E. Pepper and R.J. Elliott, J. Phys. C: Solid State Phys. 6, 1933 (1973).
6. N.E. Byer and H.S. Sack, J. Phys. Chem. Sol. 29, 677 (1968), Phys. Stat. Sol. 30, 579 (1968).
7. A.F. Devonshire, Proc. Roy. Soc. (London), A 153, 601 (1936).
8. J.J. De Yoreo, M. Meissner, R.O. Pohl, J.M. Rowe, J.J. Rush and S. Susman, Phys. Rev. Lett. 51, 1050 (1983).
9. B. Fisher and M.W. Klein, Phys. Rev. Lett. 43, 289 (1979).
10. C.W. Garland, J.Z. Kwiecien and J.C. Damien, Phys. Rev. B 25, 5818 (1982).
11. W. Hayes and R. Loudon, "Scattering of light by crystals", John Wiley and Sons Inc. (1978).
12. M.C. Hetzler, Jr., and D. Walton, Phys. Rev. B 8, 4812 (1973).
13. M. Julian and F. Luty, Ferroelectrics 16, 201 (1977).
14. T.J. Kennett, W.V. Prestwich and A. Robertson, Nucl. Inst. and Meth. 151, 285 (1978).

15. M.W. Klein, Phys. Rev. B29, 5825 (1984).

16. L. Kupferberg, Phys. Rev. B 30, 3815 (1984).

17. S.M. Lindsay, M.W. Anderson and J.R. Sandercock, Rev. Sci. Instr. 52 (10), 1478 (1981).

18. A. Loidl, R. Feile, K. Knorr and J.K. Kjems, Phys. Rev. Lett. 51, 1054 (1983), Phys. Rev. B 29, 6052 (1984).

19. A. Loidl, R. Feile and K. Knorr, Phys. Rev. Lett. 48, 1263 (1982).

20. F. Luty and J. Ortiz-Lopez, Phys. Rev. Lett. 50, 1289 (1983).

21. K.H. Michel and J. Naudts, J. of Chem. Phys. 67, 547 (1977).

22. K.H. Michel, J. Naudts and B. De Raedt, Phys. Rev. B 16, 648 (1978).

23. K.H. Michel, J.M. Rowe, Phys. Rev. B22, 1417 (1980).

24. D. Moy, J.N. Dobbs and A.C. Anderson, Phys. Rev. B29, 2160 (1984).

25. V. Narayanamurti and R.O. Pohl, Rev. Mod. Phys. 42, 201 (1970).

26. A.S. Nowick and W.R. Heller, Adv. Phys. 12, 251 (1963).

27. W.A. Phillips, J. Low Temp. Phys. 7, 351 (1972).

28. M. Prager and W. Press, J. Chem. Phys. 25, 1442 (1981).

29. J.M. Rowe, J.J. Rush, D.G. Hinkes and S. Susman, Phys. Rev. Lett. 43, 1158 (1979).

30. J.R. Sandercock, "Light scattering in Solids III", eds. M. Cardona and G. Güntherodt (1982).

31. S. Satija and C.H. Wang, Sol. St. Comm., 28, 617 (1978).

32. J.P. Sethna, S.R. Nagel and T.V. Ramakrishnan, Phys. Rev. Lett. 53, 2489 (1984).

33. J.J. Vanderwal, S.M. Mudare and D. Walton, Opt. Comm., 37, 33 (1981).

34. J.J. Vanderwal and D. Walton, Sol. St. Comm. 47, 67 (1983), Can. J. Phys. 61, 348 (1983).

35. W.M. Walsh Jr., R.J. Birgeneau, L.W. Rupp Jr., and H.J. Guggenheim, Phys. Rev. B 20, 4645 (1979).

36. D. Walton, J.J. Vanderwal and H.C. Teh, Sol. Stat. Comm., 42, 737 (1982).

37. C.H. Wang, S. Satija and F. Luty, Chem. Phys. Lett., 90, 397 (1982).